

ACCEPTED MANUSCRIPT



Protein biogenesis machinery is a driver of replicative aging in yeast

Georges E Janssens, Anne C Meinema, Javier González, Justina C Wolters, Alexander Schmidt, Victor Guryev, Rainer Bischoff, Ernst C Wit, Liesbeth M Veenhoff, Matthias Heinemann

DOI: <http://dx.doi.org/10.7554/eLife.08527>

Cite as: eLife 2015;10.7554/eLife.08527

Received: 5 May 2015

Accepted: 29 September 2015

Published: 30 September 2015

This PDF is the version of the article that was accepted for publication after peer review. Fully formatted HTML, PDF, and XML versions will be made available after technical processing, editing, and proofing.

Stay current on the latest in life science and biomedical research from eLife.
[Sign up for alerts](http://elife.elifesciences.org) at elife.elifesciences.org

1
2
3
4 **Protein Biogenesis Machinery is a Driver of Replicative**
5 **Aging in Yeast**
6
7
8

9 Georges E. Janssens^{1¶}, Anne C. Meinema^{2¶❖}, Javier González³ [‡], Justina C.
10 Wolters⁴, Alexander Schmidt⁵, Victor Guryev¹, Rainer Bischoff⁴, Ernst C. Wit³,
11 Liesbeth M. Veenhoff^{1*}, Matthias Heinemann^{2*}
12
13
14

15 1 European Research Institute for the Biology of Ageing, University of Groningen University
16 Medical Centre Groningen, Antonius Deusinglaan 1, 9713 AV Groningen, The Netherlands

17 2 Molecular Systems Biology, Groningen Biomolecular Sciences and Biotechnology Institute,
18 University of Groningen, Nijenborgh 4, 9747 AG Groningen, The Netherlands

19 3 Probability and Statistics, Johann Bernoulli Institute of Mathematics and Computer Science,
20 University of Groningen, Nijenborgh 9, 9747 AG Groningen, The Netherlands

21 4 Analytical Biochemistry, Groningen Research Institute of Pharmacy, University of Groningen,
22 Antonius Deusinglaan 1, 9713 AV Groningen, The Netherlands

23 5 Biozentrum, University of Basel, Klingelbergstrasse 50/70, 4056 Basel, Switzerland

24 [‡] Present address: Sheffield Institute for Translational Neuroscience, Department of Computer
25 Science and Department of Chemical and Biological Engineering. University of Sheffield,
26 3854A Glossop Road, S102HQ, Sheffield, UK.

27 [❖] Present address: Institute of Biochemistry, ETH Zurich, Otto-Stern-Weg 3, 8093 Zürich,
28 Switzerland

29
30 ¶ These authors contributed equally to this work.
31

32 * Co-corresponding authors:

33 m.heinemann@rug.nl (phone +31 50 363 8146, fax +31 50 363 4165)

34 l.m.veenhoff@rug.nl (phone +31 6 527 24 855, fax +31 50 361 7310)
35
36

37 **Abstract:**

38

39 An integrated account of the molecular changes occurring during the process of cellular aging is
40 crucial towards understanding the underlying mechanisms. Here, using novel culturing and
41 computational methods as well as latest analytical techniques, we mapped the proteome and
42 transcriptome during the replicative lifespan of budding yeast. With age, we found primarily
43 proteins involved in protein biogenesis to increase relative to their transcript levels. Exploiting
44 the dynamic nature of our data, we reconstructed high-level directional networks, where we
45 found the same protein biogenesis-related genes to have the strongest ability to predict the
46 behavior of other genes in the system. We identified metabolic shifts and the loss of
47 stoichiometry in protein complexes as being consequences of aging. We propose a model
48 whereby the uncoupling of protein levels of biogenesis-related genes from their transcript levels
49 is causal for the changes occurring in aging yeast. Our model explains why targeting protein
50 synthesis, or repairing the downstream consequences, can serve as interventions in aging.

51

52

53 **Introduction:**

54

55 Aging, the gradual decrease in function occurring at the molecular, cellular, and organismal
56 level, is a main risk factor for cardiovascular disease, neurodegeneration, and cancer [1].
57 Understanding its driving force is the required step towards enabling interventions that might
58 delay age-related disorders [2]. While this remains an unsolved problem in biology [3,4],
59 significant advances in the field have shown the process of aging to be malleable at both the
60 genetic and environmental levels, indicating that it is possible for its causal elements to be
61 dissected. The rate of aging, however, is influenced by diverse factors including protein
62 translation, protein quality control, mitochondrial dysfunction, and metabolism [5–8]. The
63 multitude of factors involved indicates that aging is a complex and multifactorial process, where
64 ultimately an integrated and systems-level approach might be necessary to untangle the causal
65 forces.

66

67 Important insights into the complex process of aging originate from research on the unicellular
68 eukaryote *Saccharomyces cerevisiae*, which can produce 20-30 daughter cells before its death
69 ([9] and see [10,11] for recent reviews). Significant contributions towards global mapping of the
70 aging process have been demonstrated through transcriptome studies [12–16] and genome-wide
71 single-gene deletion lifespan measurements (reviewed in [4]). However, a major task remains to
72 comprehensively describe the molecular changes that accompanies the aging process. As the
73 exponential increase in daughter cells represents a major challenge in terms of generating
74 sufficient numbers of aged cells, to date no comprehensive description of the changes on both the
75 proteome and transcriptome level has been provided. Assuming that the molecular changes
76 occurring along the replicative lifespan of yeast are in part responsible for its decreased viability
77 that occurs over time, we reason that revealing the dynamic and interdependent changes that
78 accompany this process would allow us to distinguish cause from consequence in aging.

79

80 Here, we developed a novel column-based cultivation method that generated large numbers of
81 advanced-age cells in a constant environment. Applying next-generation RNA sequencing and
82 shot-gun proteomics, we mapped the molecular phenotypes of aging yeast cells at 12 time points,

83 well into advanced age where the majority of cells had died due to aging. Analysis of these
84 dynamic and comprehensive datasets allowed us to identify a general uncoupling of protein
85 levels from their corresponding mRNA levels. This uncoupling was most apparent in protein
86 biogenesis-related proteins, which we found overrepresented relative to their transcripts. Using
87 computational network-based inference methods, we found that changes in these genes had the
88 strongest ability to predict the behavior of other genes, thereby suggesting their causal role in
89 replicatively aging yeast. On the basis of these analyses, we provide a systems-level model of
90 aging unifying and integrating diverse observations made within the field.

91

92 **Results:**

93 **Novel culture and computational methods to determine aged cell phenotypes**

94 To obtain aged yeast cells, we bound streptavidin-conjugated iron beads to biotinylated cells
95 (adapted from [17]) from an exponentially growing culture. This starting cohort of mother cells
96 was put into a column containing stainless steel mesh that was positioned within a magnetic field
97 (Figure 1A and Figure 1-figure supplement 1). The daughter cells do not inherit the iron beads,
98 as the yeast cell wall remains with the mother during mitosis [17]. By running a constant flow of
99 medium through the column, we washed away the majority of emerging daughter cells. The
100 flowing medium also provided fresh nutrients and oxygen and ensured constant culture
101 conditions, as confirmed for pH, glucose, and oxygen levels (Figure 1-figure supplement 2A, B,
102 and C). By maintaining multiple columns simultaneously, we could harvest cells from the same
103 starting cohort at different time points and thus at different replicative ages (Figure 1-figure
104 supplement 2D). Because we could retain up to 10^9 mother cells per column (Figure 1-figure
105 supplement 3), we could produce sufficient numbers of aged cells for performing parallel
106 proteome and transcriptome analyses. Computer simulations showed that the age distribution
107 broadened over time (Figure 1-figure supplement 4A, B). The broadened age distribution results
108 in a lower resolution making detecting the actual changes occurring at later time points more
109 difficult, and we therefore harvested cells at exponentially increasing time intervals to maximize
110 the differences between time points at later ages.

111

112 To assess whether our column-based cultivation method generated correctly aged cells in a
113 reproducible manner, we developed flow cytometric assays to determine the typical phenotypes
114 of aging cells. Avidin-FITC (AvF) binding to the biotin-labeled cells distinguished the starting
115 cohort of mother cells from daughter cells (Figure 1-figure supplement 5A). Dead cells were
116 identified using propidium iodide (PI), which fluoresces upon intercalating with the DNA of
117 membrane-permeable dead cells (Figure 1-figure supplement 5A). These two assays were used
118 to determine the fractions of daughters, mothers, and dead cells in a population (Figure 1-figure
119 supplement 5B). From this data, we derived the viability of the mother cells over time, which we
120 found to be in excellent agreement with the lifespan curve of yeast as observed in a microfluidic
121 device [18] (Figure 1B). Using the forward scatter of the flow cytometer as a rough proxy for
122 cell size, we could qualitatively observe the cell size increase of live mothers that is known to
123 occur in aging mother cells (Figure 1C) [19]. Similarly, using fluorophore-conjugated wheat-
124 germ agglutinin, which labels bud scars that appear after every division [20], we observed an

125 increase of bud scar staining on mother cells in the column, as also visualized by confocal
126 microscopy (Figure 1D and Figure 1-figure supplement 2D). These analyses confirmed known
127 changes that characterize aging yeast: increased cell size, increased bud scars, and decreased
128 population viability (Figure 1B, C, and D).

129
130
131 Next, we developed a combined experimental and mathematical method to determine the
132 molecular phenotype of aging mother cells without contributions from daughter or dead cells.
133 The approach exploits the fact that a system of linear equations can be solved when the number
134 of unknowns equals the number of independent equations. Specifically, while we could
135 determine the number of mothers, daughters, and dead cells in a sample using flow cytometry,
136 the contribution of each type of cells to the measured abundance of a particular protein or
137 transcript was unknown. Therefore, by measuring protein and transcript abundances in three
138 mixed samples with various proportions of mothers, daughters, and dead cells, we could
139 mathematically unmix the abundances. This resulted in unmixed data for the aging mother cells.
140 Experiments using samples with mixed cell populations with known molecular phenotypes
141 validated this mathematical unmixing method for the RNAseq transcriptome, targeted (selected
142 reaction monitoring) proteome, and global (shotgun) proteome data with a <16% average error
143 (Figure 2-figure supplement 1 and 2; supplemental note 1).

144
145 To use this data unmixing approach, we harvested three mixed samples for each time point
146 (Figure 2A, Figure 2-figure supplement 3). One sample was collected from the column effluent
147 (Mix 3, mainly daughter cells). Harvesting all cells from the column and applying a further
148 enrichment step on a larger magnet produced the two other samples: one sample contained
149 mainly aged mother cells (Mix 2, 80–99% mothers), while the other contained an intermediate
150 composition compared to Mixes 2 and 3 (wash fraction, Mix 1). In each of these mixed-cell
151 samples, we determined the fraction of mothers, daughters, and dead cells and generated the
152 mixed-population proteomes and transcriptomes. Then, we mathematically unmixed the
153 proteomes and transcriptomes to obtain the molecular phenotype of aging mother cells. The data
154 was corrected for sampling artifacts related to bead labeling and cell harvesting (Figure 2-figure
155 supplement 4 and supplemental notes 2 and 3). Together, through this approach, we obtained
156 pure data for aging mother cells and daughter cells.

157
158 In two experimental series with overlapping time points, we generated 61 samples for both the
159 proteome and the transcriptome as required for unmixing. After data processing, we obtained
160 high quality data at 12 unique time points during the lifespan of replicatively aging yeast (Figure
161 2-figure supplement 5). We found the replicates to be in excellent agreement (Spearman
162 correlations > 0.85) (Figure 2B and C). A unified data set was generated for both the proteome
163 and the transcriptome by fitting the replicate datasets with a polynomial regression (Figure 2D
164 and E), keeping highly reproducible data profiles (~85% of genes, Figure 2-figure supplement 6),
165 and resampling the fit at the actual time points of the experiment. This yielded profiles for 1494
166 proteins and 4904 transcripts from aging mother cells. The raw data [22,23] and the data for each
167 processing step are provided in the supplementary Tables S2 and S3 (Figure 2-source data 1 and
168 2). The final datasets for aging mother cells are presented in Table S4 (proteome) and Table S5
169 (transcriptome) (Figure 2-source data 3 and 4).

170

Biogenesis proteins increase relative to transcript levels during aging

Correlation analyses between the proteomes of young cells and the proteomes of aging mother cells confirmed the expected divergence of the aging cell away from the youthful state (Figure 3A and Figure 3-figure supplement 1). Daughters from later time points showed a partially aged signature (Figure 3-figure supplement 2), consistent with the notion that rejuvenation of daughter cells is incomplete later in a mother's life [24]. Furthermore, we found agreement between specific proteome changes detected by us and observations present in literature, including changes related to glycolysis, and gluconeogenesis [13], increased expression levels in energy reserve pathway proteins [25], increases in stress response protein levels [26,27], and mitochondrial changes [28] (Figure 3B, Figure 3-figure supplement 3). Also, we confirmed that changes detected in our population-level study similarly occurred at the single-cell level, which excluded the possibility that our observed changes may reflect a gradual enrichment of a long lived subpopulation. Specifically, we see the levels of the stress-related chaperone Hsp104 and the translation elongation factor Tef1 to increase with age (Figure 3-figure supplement 4), similar to what was shown using a microfluidic platform tracking single cells [29]. Also, other single protein changes reported to occur in literature match well [15,21,28–33] (Figure 3-figure supplement 4). Together, these observations confirm the validity of our novel experimental design.

To obtain further insights into the global changes in protein expression in mother cells, we plotted our dynamic data as a heat map expression profiles. We found that changes started at young age, were gradual, and mostly occurred in one direction (i.e. up, down) (Figure 4A and B). Specifically, we found that 64% (184/288 total changes) of the proteins that showed a 2-fold change by the end of the yeast lifespan also showed a significant change in the same direction at an earlier time point (Figure 3B). These findings suggest that aging is a gradual process occurring from early on.

We next investigated whether these changes in the proteome data matched transcriptional changes. Interestingly, the RNAseq data showed similar gradual and unidirectional changes occurring from the beginning on (Figure 4-figure supplement 1A, 2, 3). To compare the changes between the proteome and transcriptome, we determined the non-parametric Spearman rank correlation, and found a starting correlation of 0.75, a value in agreement with other single-study comparisons between yeast proteomes and transcriptomes [34]. When comparing this correlation in time, however, we found that it declined steadily with age, down to a correlation of 0.70 (Figure 5A). This decreasing trend was observed regardless of the statistical method used (Figure 5-figure supplement 1). Furthermore, this trend is also not an experimental artifact, since samples originating from all time points were treated identically, and both proteome and transcriptome datasets originated from the same biological samples. The decrease in correlation between the proteome and transcriptome means that they do not change synchronously. Indeed, during aging, we found different GO terms to describe the changes in the proteins and transcripts that show a larger than 2-fold change during aging (Figure 3B vs. Figure 4-figure supplement 2A). These results indicate that, over time, protein levels were increasingly uncoupled from their transcript levels.

216 To identify the most uncoupled cellular processes, we plotted the fold-changes of transcript and
217 protein expression in old and young cells on a gene product co-expression map (Figure 5A). The
218 transcript and protein levels of genes in quadrants 1 (Q1) and 3 (Q3) were ‘coupled’, meaning
219 that the changes in protein levels followed the changes in transcript levels. Q1 and Q3 were
220 enriched in gene products related to sterol biosynthesis and cytoskeletal and cell wall processes,
221 possibly related to cell growth. In contrast, the expression of gene products in quadrants 2 (Q2)
222 and 4 (Q4) were ‘uncoupled’, meaning that the changes in protein levels did not follow the
223 changes in transcript levels. In Q2, the proteins were overrepresented relative to their transcripts,
224 i.e. there were more proteins per transcript in older cells than in younger cells. Of all analyzed
225 transcript-protein pairs, 38.4% were located in Q2, suggesting a global tendency towards relative
226 protein overabundance with aging (Figure 5). In line with this global protein overabundance, Q4
227 contained fewer genes and less GO-term enrichments. Strikingly, Q2 was strongly enriched in
228 ‘translation regulation’ gene products (i.e. ribosome and protein biogenesis machinery) (Figure
229 5B), and the extent of their overabundance progressively increased as the cells aged (Figure 5-
230 figure supplement 2, 3).

231

232 **Network inference identifies protein biogenesis related genes as causal in yeast aging**

233

234 Next we asked whether this increased level of biogenesis-related proteins, uncoupled from
235 transcriptional regulation, was causal for downstream effects during replicative aging in yeast.
236 Identifying causality on a systems-wide level is difficult, and the key challenge is to separate
237 cause from downstream effects. However, our dynamically resolved, comprehensive data offered
238 the possibility to reveal causal relationships.

239

240 To elucidate the causal order of changes during aging, we reconstructed a high-level directional
241 network revealing the interdependences of changes in transcript expression (Figure 6, Figure 6-
242 figure supplement 1A). Therefore, we defined each transcript’s expression profile as a network
243 node, and an edge between each pair of nodes as a partial correlation between the nodes’
244 expression profiles (Figure 6-figure supplement 1B and C). Next, we determined the
245 directionality of the edges, indicated by arrows. We defined directionality to represent the ability
246 of a transcript’s profile to predict the profile of another transcript. Concretely, when looking at
247 two connected nodes, the node that could be explained by the connected node was considered as
248 the responsive node, while the predicting node was considered to be the causal node. (Figure 6-
249 figure supplement 1D and E) [35]. This relation defined the directionality of the edge. Any
250 transcript that had no predictive ability and could not be predicted by any other transcript was
251 removed from the network analysis. Following this, the nodes were clustered by maximizing the
252 global modularity of the network [36] (Figure 6A and Figure 6-figure supplement 1). Finally, the
253 clusters were ranked based on the ratio of causal nodes (outward arrows) to responsive nodes
254 (inward arrows) per cluster to determine the higher-level causal relations existing between
255 clusters. A sensitivity analysis was performed to determine the optimal sparsity of the network
256 and the cut-off for the partial correlation among transcript profiles, through which we established
257 that the network was a robust representation of the datasets (supplemental note 4, Table S7
258 Figure 6-source data 1). These steps produced a high-level directional network, in which the
259 ranking of the clusters with respective GO enrichments revealed causal relations during aging
260 (Figure 6B).

261

262 This high-level directional network of the transcriptome data showed that the very first causal-
263 ranked cluster in the network that we detected was highly enriched for gene products associated
264 with protein biogenesis (i.e. ribosome biogenesis and tRNA processing; Figure 6B). These are
265 the same biological processes that had uncoupled transcript and protein levels (Figure 5B);
266 indeed, genes from this causal cluster were enriched in Q2 of the co-expression map, which
267 showed uncoupled expression (Figure 6-figure supplement 2A and B). These analyses suggest
268 that the uncoupling of protein and transcript levels for ‘biogenesis’ related genes has a central
269 role in the aging process, and may affect the transcript and protein abundances of other genes, as
270 elaborated upon in the discussion.

271

272 **Consequences for other cellular processes**

273

274 The overabundance of proteins relative to transcripts must have consequences for cellular
275 functioning. Protein overproduction could increase cell size, one of the first hallmarks described
276 in yeast aging [19]. Increased cell size could reduce glucose influx rates per cell volume and
277 induce metabolic changes, e.g. at low rates of glucose influx cells switch to respiration [37].
278 Indeed, in our transcript-based network analysis (Figure 6B) as well as in our proteome data set
279 (Figure 3B) we found that metabolic signatures related to starvation and oxidative stress were
280 consequences of aging.

281

282 Furthermore, we hypothesized that if protein levels become globally uncoupled from their
283 transcript levels during aging (Figure 5), the optimal stoichiometry of proteins in complexes may
284 be perturbed (Figure 7A). Indeed, using curated lists of protein complexes [38], we found that an
285 increased deviation from the original stoichiometry occurred with aging (Figure 7B, C and D,
286 and Figure 7-figure supplement 1, 2 and 3). We observed many complexes that were not
287 previously implicated in aging to be age-affected, and we found previously implicated protein
288 complexes such as the vacuolar ATPase [28] and the nuclear pore complex [30,31] to lose
289 stoichiometry (Figure 7C and D and Figure 7-figure supplement 1, 2). The global stoichiometry
290 loss was greater in aged mothers compared to the daughter population (Figure 7-figure
291 supplement 3A), confirming that this is an aging-related phenotype. Additionally, we found that
292 the stoichiometry loss was greater overall at the proteome level than at the transcriptome level
293 (Figure 7B), supporting the observation that protein levels uncouple from their transcript levels.

294

295 Being built of fewer genes (1494 proteins versus 4904 transcripts), the high-level directional
296 network of the proteome was less revealing than that of the transcriptome (Figure 7-figure
297 supplement 4). The most causal cluster of the proteome network was enriched for chaperone
298 proteins, reflecting a cellular response to internally changing conditions. Such conditions could
299 include metabolic restructuring in response to an increased cell size or to aggregating proteins
300 that are accumulating due to altered protein complex stoichiometry. Furthermore, we found that
301 the causal clusters of the proteome network tended to be expressed according to their
302 transcriptional message (i.e. coupled expression; Q1, Q3), while the responsive clusters
303 represented increasingly uncoupled expression (Q2, Q4) (Figure 6-figure supplement 2C). This
304 both confirmed the response of the cell to the accumulating changes occurring during aging and
305 indicated that the effects of uncoupled protein expression are progressive over time. We see the
306 clear downstream consequences during aging emerging in the proteome, including metabolic
307 shifts, stoichiometric loss, aggregating proteins, and protein overproduction. All of these point to

308 pathways and processes that may become dysfunctional with aging, any of which may ultimately
309 result in cell death.

310

311

312 **Discussion:**

313

314 Using our newly developed culturing and computational methods and state-of-the-art proteomics
315 and transcriptomics analyses, we generated the first systems-level molecular phenotype of
316 replicatively aging yeast. The comprehensiveness of the data allowed us to discover that protein
317 biogenesis machinery genes, including ribosome, tRNA synthesis, and translation regulation
318 genes, have their protein levels uncoupled from their mRNA levels during aging (Figure 5B).
319 Furthermore, the dynamic nature of the data allowed us to pinpoint the transcripts of these genes
320 as having the strongest ability to predict the behavior of others transcripts during aging (Figure
321 6B). Lastly, we observe metabolic changes, protein stress responses, and changes in the
322 stoichiometry of many protein complexes (Figure 3B, 4, 7B).

323

324 Based on these analyses we propose a model whereby the uncoupling of protein levels of
325 biogenesis-related genes from their transcript levels is causal for the changes occurring in aging
326 yeast. The model proposes that proteins of the translation machinery that are uncoupled from
327 transcript levels accumulate in cells with age (Figure 5B). As the biogenesis genes are themselves
328 involved in translation, their uncoupling might contribute to further uncoupling of the proteome
329 from the transcriptome as a whole. This general uncoupling has degenerative effects (i.e. cell
330 size increase, protein aggregations and loss of stoichiometry in protein complexes), that stimulate
331 transcriptional responses in the cell (i.e. metabolic changes and activated stress responses),
332 which further contributes to changes in the proteome. Although we cannot exclude the possibility
333 of other causes even further upstream, the uncoupling of the protein biogenesis machinery is
334 likely an early driver of replicative aging in yeast.

335

336 A question remains as to why the biogenesis-related class of proteins we identified as having
337 protein levels uncoupled from their transcript levels become overrepresented in replicatively
338 aging yeast in the first place. Ribosome footprinting has shown these proteins to be highly
339 translated [39], and turnover experiments have shown them to be highly stable [40]; thus, it is
340 possible that their overabundance may result from the combination of the dynamics of protein
341 biogenesis, protein turnover, and mRNA stability. Interestingly, the ribosomal proteins
342 themselves showed a low degree of loss of stoichiometry at the protein-complex level in our data
343 (Figure 7C), supporting the idea that they are still active and contributing to uncoupling in the
344 cell. In any case, the uncoupling of protein and transcript levels has downstream consequences
345 for the cell that may explain many phenotypes of aging. First, cell size may increase due to
346 protein overproduction and result in metabolic changes. Second, proteins being overproduced at
347 different rates will alter protein complex stoichiometry. Many documented phenotypes of aging
348 may result from this, including the formation of protein aggregates [26], increased ROS
349 formation by a dysfunctional mitochondrial transport chain [41], and loss of gene silencing [42].
350 The sum of these may ultimately lead to system failure for the organism.

351

352 Directly targeting certain failing protein complexes or downstream deleterious effects results in
353 replicative lifespan extension, but we suggest that many of these effects will prove to be cell

354 type- and growth condition-specific. Our model predicts that a more robust extension of lifespan
355 may be possible in many organisms by targeting the causal factor in aging, protein biogenesis.
356 Indeed, altering the rates of protein production (i.e. translation) or degradation (i.e. autophagy)
357 have repeatedly been shown to influence longevity across a wide range of organisms (see
358 [10,43,44]). The translation activators TOR and S6 kinase fall into this category, and decreases
359 in their activity result in increased lifespan in yeast [45,46], worms [47,48], flies [49], and mice
360 [50,51], as does calorie restriction and drugs such as rapamycin, which are also modulators of
361 protein biogenesis pathways [43]. Likewise, deletions in ribosomal subunit components have
362 positive effects on lifespan in both yeast [52] and worms [53]. Our model suggests why these
363 interventions and mutations have a lifespan-extending effect in a broad spectrum of organisms,
364 namely because protein biogenesis machinery is itself a driver of aging.

365
366

367 **Materials and methods:**

368

369 Aging Yeast

370

371 *Strains and medium*

372 The prototrophic *Saccharomyces cerevisiae* strain YSBN6 (Mata) was used for the
373 phenotyping of yeast replicative aging [54]. The cells were grown in yeast nitrogen base (YNB)
374 without amino acids (ForMedium, Norfolk, UK) supplemented with 2% glucose, at a
375 temperature of 30°C, unless indicated differently. Precultures in flasks were shaken at 300 RPM.

376 Replicates of samples not processed by the steps involving biotinylation and the
377 attachment of beads (termed “unprocessed samples”) were precultured in the above medium for
378 minimum 24 hours in mid exponential growth phase and were immediately pelleted (5 min
379 2500×G) and snap frozen in liquid nitrogen.

380

381 *Preparing the cells for column captured culturing in aging columns*

382 Prior to loading the cells onto the aging columns, the cells were biotinylated and labeled
383 with iron beads (Figure 1–figure supplement 1) in a manner adapted from [17], as follows: The
384 yeast YSBN6 was pre-cultured for minimally 24 hours in a mid-exponentially growing growth
385 phase, having an OD₆₀₀ below 1. Cells were harvested and concentrated by gently centrifugation,
386 10min 2500×G. For one column, 3×10⁹ cells were resuspended in 1 ml 2×PBS (phosphate
387 buffered saline), immediately mixed with 14 mg Sulfo-NHS-LC-Biotin (Thermo Scientific,
388 Rockford, IL, USA) dissolved in 1 ml cold (4°C) water and incubated in a shaker (800 rpm) at
389 room temperature for 20 minutes. The biotinylated cells were washed twice with 1×PBS at room
390 temperature and were resuspended in 100 ml pre-warmed YNB plus 2% glucose and incubated
391 for 90 minutes at 30°C shaken at 300 RPM. At room temperature, the cells were pelleted by
392 gentle centrifugation (5min, 2500×G), washed with 1×PBS, resuspended in 4 ml 1×PBS, mixed
393 with 750 µl of streptavidin coated BioMag beads (Qiagen, Germantown, MD, USA) and
394 incubated for 30 min on a lab rocker. The bead-labeled cells were concentrated in ~0.5 ml PBS
395 by gentle centrifugation (5min, 2500×G) and 2×10⁹ cells were loaded onto the magnetized aging
396 column.

397

398 *The aging columns setup*

399 The aging column setup is a closed system, where cells are cultivated on a magnetized
400 iron meshwork under a constant flow of medium (Figure 1–figure supplement 1B and C). The
401 setup was designed to ensure a sterile environment within the system, continuous removal of
402 daughter cells, and constant oxygen and nutrient concentrations in the medium. Table S1 (Figure
403 1-source data 1) shows materials used for its construction and operation.

404 The core of the setup for column captured cell cultivation is the 0.3" Negative Selection
405 Column combined with a 3-way stopcock (Stemcell Technologies Inc., Figure 1-source data 1
406 Table S1), which is placed in a magnetic field. Four magnets (StemSep™ Red Magnet, Stemcell
407 Technologies) were placed in a stand (custom made, Figure 1–figure supplement 1D), and four
408 stands with magnets were connected in a row to run 16 columns simultaneously. The rim at the
409 top of the column was cut with a sharp scalpel, to enable connection with 15 cm long silicone
410 tubing (Si, inner diameter (id) 8mm, outer diameter (od) 11mm, Si 8-11, Figure 1–figure
411 supplement 1C, Figure 1-source data 1 Table S1). Silicone tubing was chosen, as it is air
412 permeable. The T-connector (od 10 mm, C T-10) on top serves to connect the column with the
413 inlet tubing from the side and a 6 cm long tubing closed with a clamp (C.II).

414 The pump (BVP standard motor, MS/CA4-12 + 3× MS/CA4-12 extensions; Ismatec)
415 provided a constant medium flow over the column. The pump tubing (Pharmed, BPT Tubing,
416 1.52 mm ID, 400 mm length) connected the 20L medium jar (20L round HDPE bottle, Nalgene)
417 to the column via 2 long pieces of 2m silicone tubing (id 2 mm, od 4 mm, Si 2-4). The Silicone
418 tubing between pump and column could be closed with clamp C.II. The flow rate of medium
419 over the column was set at 170 ml/h.

420 The medium jar was closed with a 5-layered aluminum foil top prior to autoclaving. 5
421 syringes with their plungers removed were punched through the aluminum foil and 4 were
422 connected inside the jar to a 60 cm long silicone tubing (id 6 mm, od 8 mm, Si 6-8). The end of
423 the tubing was weighted down with a glass pipet, in order to have the inlet remain at the bottom
424 of the jar. The syringe barrels at the top of the jar were closed with small pieces of aluminum foil
425 during autoclaving and attached to the Si 2-4 silicon inlet tubing prior to the start of the column
426 run. The fifth syringe without its plunger and without silicon tubing was attached on the outside
427 to Si 2-4 silicone tubing, with pressurized sterile air, to provide an overpressure of sterile air in
428 the medium jar. The medium jar was filled with 20L autoclaved Yeast Nitrogen Base without
429 amino acids (YNB) prior to autoclaving and was subsequently supplemented with 2% filter
430 sterilized glucose.

431 The effluent of the column goes down via silicone Si 2-4 tubing, passes a quick release
432 connector, and goes up via silicone Si 4-6 tubing to an air chamber. The tubing can be closed
433 with a clamp (C.III). The air chamber breaks the laminar medium flow, allowing the liquid to
434 drip down via silicone Si 4-6 tubing into a waste jar (20L round HDPE bottle, Nalgene). The air
435 chamber consists of a T-connector (od 10 mm, C T-10) connected at all 3 sides with 6 cm
436 silicone Si 8-11 tubing and a tube connector.

437

438 *Loading the aging columns*

439 Prior to loading the columns with the biotinylated yeast cells, the system was primed with
440 sterile medium for about 1 hour, having clamp C.I and C.III open. The medium flow was then
441 stopped on the pump and clamps C.I and C.III were closed and clamp C.II opened. The quick
442 release was opened and clamp C.III was shortly opened to lower the medium level to the iron
443 meshwork. The column was detached from the tubing and the magnet and 2×10^9 cells were
444 pipetted onto the column and gently sucked into the meshwork by a 5 ml syringe attached to the

445 stopcock below the column. The stopcock was closed, ~2ml fresh medium was pipetted on top of
446 the column and the column was reattached to the tubing and placed in the magnet. Clamp C.I
447 was opened and the medium flow was restarted. After some medium was collected on top of the
448 column, clamp C.III was opened. Clamp C.II was kept open until the medium level above the
449 column stabilized halfway in the tubing above the column. This level could be adjusted by the
450 height of the air chamber in the effluent tubing (Figure 1–figure supplement 1B). The cells were
451 kept surrounded by liquid media throughout all cultivation time.

452

453 *Harvesting aged yeast cells*

454 In order to harvest mother cells, the pump was stopped, clamps C.I and C.III were closed
455 and clamp C.II opened. Only the specific pump tubing was disconnected from the pump, and the
456 pump was restarted. The quick release was disconnected and by shortly opening clamp C.III, the
457 medium level was lowered to just above the meshwork. The tubing on top of the column was
458 detached and a 20 ml syringe was connected to the stopcock below the column. While keeping
459 the column at the magnet, 15 ml fresh medium was provided on top of the column, while the
460 column effluent was collected by the syringe. This step was repeated for 2 or 3 times, until the
461 effluent was clear. This combined column effluent sample was kept on ice (effluent fraction,
462 sample: Mix 3, Figure 2–figure supplement 3A). The column was detached from the magnet and
463 again 15 ml fresh medium was provided on top of the column and the effluent was collected by a
464 new syringe. This was repeated 2 or 3 times, until the medium was clear. This combined column
465 fraction (column fraction, later to be split into Mix 1 and 2, Figure 2–figure supplement 3A) was
466 also kept on ice.

467 After harvesting, the samples consisted of mixes of aged mother cells, dead cells, and
468 daughter cells. In order to obtain a higher purity of aged mother cells, an enrichment step was
469 required for the column fraction. The cells were gently centrifuged (10 min 2500xG),
470 resuspended in 7 ml cold PBS and transferred to a glass test tube. The test tube was placed in a
471 magnet ("The Big Easy" EasySep™ Magnet, Stemcell technologies Inc.) for 5 minutes (Figure
472 2–figure supplement 3A, panel II). The supernatant was removed by pipetting and the magnet
473 bound cells were resuspended in fresh and cold PBS. This was repeated 2 times, at which time
474 the supernatant was clear. The supernatant fractions were combined and kept on ice (wash
475 fraction, sample: Mix 1). The cells that were retained in the magnet were resuspended in 2 ml
476 PBS after removal from the magnet (mother enriched fraction, sample: Mix 2) (Figure 2–figure
477 supplement 3A, panel III). The samples were pelleted by gentle centrifugation (4 min, 4°C,
478 2500×G) and immediately snap frozen in liquid nitrogen. A small aliquot of each of three
479 samples was kept aside to measure the fractions of live and dead cells, mother and daughter cells,
480 and to obtain the cell count per sample.

481

482 *Harvesting timepoints*

483 Based on the population viability curves generated from the columns during test campaigns,
484 the average lifespan of yeast being roughly 20-30 divisions, and the doubling time of the YSBN6
485 strain being roughly 2 hours, it was decided to collect aged samples up to 72h of aging, with
486 roughly 42% of viable cells expected in the last sample (Figure 1B). There is cell-to-cell
487 variation in the replication rates of yeast and so with time the distribution of replicative ages per
488 sample increase. These distributions were modelled based on the variation of the replication rates
489 as quantified from single cell microfluidic data (unpublished data). In a mathematical model, a
490 start culture of 1000 cells having a random replication rate according to a Poisson distribution

491 around an average replication rate of $0.5h^{-1}$ was allowed to replicate (and age) in time (Figure 1–
492 figure supplement 4). Consistent with our empirical observations counting bud scars in the
493 population (Figure 1–figure supplement 2D), with increasing elapsed time, the distributions of
494 the number of replications per cell became wider. Linearly spaced harvesting in time would
495 cause increasing information overlap between neighboring time points, thus it was decided to
496 harvest samples exponentially spaced in time (Figure 1–figure supplement 4).

497 Finally, we performed two replicate runs of the column captured cell culturing campaigns.
498 Campaign 1 generated an unprocessed sample and 14 column samples and replicate campaign 2
499 generated another unprocessed sample and 8 column samples. In total, two unprocessed samples
500 combined with 16 unique time points were generated (Figure 2–figure supplement 5).

501

502 *Flow cytometry analysis of sample composition*

503 In each sample the cells were counted on a BD Accuri™ C6 flowcytometer (Becton,
504 Dickinson and Company, New Jersey, USA). To quantify the fractions of mother cells, dead
505 cells, and daughter cells in the samples, the cells were stained with dyes and analyzed by flow
506 cytometry using the BD Accuri™ C6. From each aliquot, 2×10^6 cells were pelleted and
507 resuspended in 100 μ l PBS, and simultaneously stained for 30 min at room temperature with 5 μ l
508 5mg/ml Fluorescein conjugated Avidin (AvF, Thermo Scientific, Rockford, USA) and 2 μ l 2mM
509 Propidium Iodide (PI, Fluka/Sichma-Aldrich Co., St. Louis, MO, USA). Mother cells, which are
510 biotinylated (see section Materials and methods, Preparing the cells for column captured
511 culturing in aging columns), were stained with AvF, dead mother or dead daughter cells were
512 stained with PI, live daughter cells remained unstained (Figure 1–figure supplement 5). The
513 Fluorescein was excited by a laser of 488 nm wave length and detected in the range of 533 +/- 30
514 nm, PI was excited by a laser of 488 nm and detected in the range of >670 nm. The beads were
515 excluded from any analysis by gating (Figure 1–figure supplement 5B, left panels). The flow
516 cytometer events were plotted for their PI and AvF intensities in a scatter plot, clear clusters for
517 stained and unstained, both in PI and AvF channel, were apparent. The fractional enrichments
518 were obtained in the BD CS Accuri™ C6 Software 1.0 (Figure 1–figure supplement 5).

519

520 *Validations of column captured cultivation*

521 *Oxygen concentration in medium:* The oxygen concentration was measured by using the
522 Optical Oxygen Meter Fibox 3 (PreSens - Precision Sensing GmbH, Regensburg, Germany). The
523 flow-cell, an oxygen-sensitive spot glued in a polystyrene tube, was connected to tubing in front
524 of the aging column, to measure the O₂ concentration in fresh medium and connected to the
525 effluent tubing, to measure the O₂ concentration in the column effluent. Each measurement was
526 done within 10 minutes to avoid that the measurements were influenced by the accumulation of
527 yeast cells in the flow-cell, which would alter readings.

528 *Glucose consumption on the column:* The glucose concentration in the medium and in the
529 column effluent was measured with a commercially available enzyme-based assay Enzytec™
530 fluid D-Glucose (Thermo Fisher Scientific GmbH). The column effluent samples were harvested
531 by collecting medium from the column outlet, by opening the quick release below the column
532 (Figure 1–figure supplement 1B and C). The column effluent sample was immediately placed on
533 ice, shortly centrifuged (30s, >16k \times G) to remove the cells, and the glucose concentration was
534 measured.

535 *Bud scar counting:* The number of bud scars was counted using microscopy and
536 evaluated from flow cytometry data.

537 For microscopy, 1×10^7 cells were resuspended in 0.5 ml PBS supplemented with 25 μ l
538 5mg/ml Alexa 633 labeled wheat germ agglutinin (WGA, Life Technologies), 50 μ l 5 mg/ml
539 AvF and 20 μ l 2mM PI and incubated for 90 min at room temperature (see “Flow cytometry
540 analysis of sample composition”). The images were taken on a commercial laser scanning
541 microscope Zeiss LSM710 (Carl Zeiss, MicroImaging, Jena, Germany), using ZEN2010B
542 software. The dyes were excited with different solid state lasers; PI and AvF were excited with a
543 wavelength of 488 nm and emission was recorded between 607 – 797 and 493 – 564 nm
544 wavelength, respectively; WGA-Alexa 633 was excited, with a wavelength of 633 nm and
545 emission was recorded between 638 – 797 nm wavelength in a stack of 10 images with a z-
546 scaling of 0.8 micrometer (Figure 1D, inset). Only living mother cells were selected (containing
547 AvF, without PI) and the bud scars were counted independently by two researchers.

548 For flow cytometry, 2×10^6 cells were resuspended in 100 μ l PBS supplemented with 7 μ l
549 5mg/ml WGA-Alexa 633 and incubated for 30 min at room temperature. The cells were excited
550 in the flow cytometer by a laser with 640 nm wavelength and emission was recorded with a filter
551 selecting for 675 \pm 25 nm. The mean fluorescence intensity for R2 is normalized to R1 t = 0h, to
552 be plotted on the same scale (Figure 1D).

553 *Life span curve:* For viability of mother (Avidin-FITC positive) and daughter (Avidin-
554 FITC negative) cells at each time point in the aging column, viability of the mother and daughter
555 cells was assessed in each mixed-cell sample (derived from proportions of live (PI negative) and
556 dead (PI positive) cells (Figure 1-figure supplement 5, Figure 2-figure supplement 3B)). These
557 scores were weighted based on the number of cells present in each of these samples (derived
558 from raw numbers as presented in Figure 1-figure supplement 3). This ensures that the viability
559 of mothers and daughters (Figure 1C) reflects the entire population, since mothers and daughters
560 in different mixed-cell samples may have slightly different ratios of live to dead cells. The
561 microfluidic based lifespan curve was obtained from authors of [18], based on 2641 cells, plotted
562 as viability versus time.

563
564

565 Proteome analysis

566

567 ¹⁵N standards

568 Protein extracts from isotopically labeled ¹⁵N YSBN6 yeast cells were used as an internal
569 standard for the targeted Selected Reaction Monitoring (SRM) proteomics experiments. For the
570 preparation of the ¹⁵N standards, yeast was cultivated in two 2.5L-fermentors on minimal or
571 synthetic Verduyn medium [55], supplemented with 10 g/L glucose and using ¹⁵N-labeled
572 (NH₄)₂SO₄ as the sole nitrogen source. Cells were harvested in the different growth phases,
573 namely the log phase (L), the deceleration phase (D) and the stationary phase (S, Figure 2-figure
574 supplement 1A). Aliquots from all conditions were mixed (1:1:1) to maximize the coverage of
575 targeted proteins.

576

577 Cell lysis and protein extraction

578 Cell pellets were resuspended in 1.85M sodium hydroxide plus 7.4 % v/v β -mercapto-
579 ethanol at a concentration of 1×10^8 cells per 100 μ L and incubated for 10 minutes on ice. An
580 equal volume of 100% w/v trichloric acid (TCA) was added and was subsequently incubated 10
581 minutes on ice. The precipitated proteins were collected by centrifugation (16k \times G, 10 min, 4 $^{\circ}$ C).

582 The pellet was washed with 200 μ L cold acetone and incubated for 30 min at -20 °C. Finally, the
583 protein pellet was collected by centrifugation (16 \times G, 10 min, 4 °C), and removal of supernatant.
584 The precipitated proteins were resuspended in 100 μ l 2% w/v sodium deoxycholate plus 100 mM
585 ammonium bicarbonate (ABC) per 1 \times 10⁸ cells. For the targeted proteomics the ¹⁵N-labelled
586 protein extracts were added in a 1:1 ratio, based on the cell counts. Samples were incubated for 5
587 minutes at 90°C to solubilize. Magnetic beads present in a subset of the samples were removed at
588 this stage by collecting them on the commercially available magnet tube rack DynaMag™-2
589 (Life Technologies/Thermo Fisher Scientific Co. Carlsbad, California, United States).

590

591 *Digestion and cleanup*

592 The solubilized proteins were reduced with 12 mM dithiothreitol (30 min at 55 °C) and
593 alkylated with 40 mM iodoacetamide (45 min at 30 °C, in the dark). Samples were diluted with
594 100 mM acetonitrile (ABC) to dilute the sodium deoxycholate to 1% w/v prior to overnight
595 digestion with trypsin (1:100, sequencing grade modified trypsin V5111, Promega) at 37 °C.
596 Then, 10% v/v formic acid (FA) was added to the solution to precipitate the deoxycholate, which
597 was subsequently removed by centrifugation (16k \times G, 10 minutes). Cleanup prior to LC-MS
598 analysis was done with C18-SPE columns (SPE C18-Aq 50 mg/1ml, Gracepure). This column
599 was conditioned with 3 \times 1 ml ACN plus 0.1% v/v FA, and re-equilibrated with 3 \times 1 ml 0.1% v/v
600 FA before application of the samples at a total amount of maximally 1 mg total protein per
601 column. The bound peptides were washed with 2 \times 1ml 0.1% v/v FA and eluted with 3 \times 0.4 ml
602 50% v/v ACN plus 0.1% v/v FA. The eluted fractions were dried under vacuum and resuspended
603 in 0.1% v/v FA to a final concentration of around 1 μ g/ μ l.

604

605 *Targeted proteomics (SRM)*

606 SRM analyses were performed on a triple quadrupole mass spectrometer with a
607 nanoelectrospray ion source (TSQ Vantage, Thermo Scientific). Chromatographic separation of
608 the peptides was performed by liquid chromatography on a nano UHPLC system (Ultimate
609 UHPLC focused, Dionex) using a nano column (Acclaim PepMap100 C18, 75 μ m \times 150mm 3 μ m,
610 100 Å). Samples were injected at a total amount of 1 μ g using the μ l-pickup system using 0.1%
611 v/v formic acid as transport liquid from a cooled autosampler (5 °C) and loaded onto a trap
612 column (μ Precolumn cartridge, Acclaim PepMap100 C18, 5 μ m, 100 Å, 300 μ m id, 5 mm
613 Dionex). Peptides were separated on the nano-LC column using a linear gradient from 3-45 %
614 v/v ACN plus 0.1% v/v formic acid in 30 minutes at a flowrate of 0.3 μ l/min. The mass
615 spectrometer was operated in the positive mode at a spray voltage of 1500V, a capillary
616 temperature of 270 °C, a half maximum peak width of 0.7 for Q1 and Q3, a collision gas
617 pressure of 1.2 mTorr and a cycle time of 1.2 ms. The measurements were scheduled in windows
618 of 4 minutes around the pre-determined retention time, with a maximum of 150 concurrent
619 transitions.

620 The MS traces were manually curated using the Skyline software [56]. The sum of all
621 transition peak areas for the endogenous and standard (¹⁵N labeled) peptide was used to calculate
622 the ratio between the endogenous and standard peptides. Only peptides that were minimally
623 quantified with two transitions and with a peak area of the ¹⁵N standard above 10.000 for both
624 technical replicates were considered for quantification. The ratios on protein level were
625 calculated by averaging the ratio of all peptides per protein. In order to correct for global errors
626 made in the protein concentration determination of either the endogenous samples or the ¹⁵N
627 labeled standard, the median of all datasets were normalized to the same value.

628 *Shotgun proteomics*

629 1 µg of peptides of each sample were subjected to LC–MS analysis using a dual pressure
630 LTQ–Orbitrap Velos mass spectrometer connected to an electrospray ion source (Thermo Fisher
631 Scientific) as described recently [57] with a few modifications. In brief, peptide separation was
632 carried out using an EASY nLC-1000 system (Thermo Fisher Scientific) equipped with a RP-
633 HPLC column (75 µm × 45 cm) packed in-house with C18 resin (ReproSil-Pur C18–AQ, 1.9 µm
634 resin; Dr. Maisch GmbH, Ammerbuch-Entringen, Germany) using a linear gradient from 95%
635 solvent A (0.15% formic acid, 2% acetonitrile) and 5% solvent B (98% acetonitrile, 0.15%
636 formic acid) to 28% solvent B over 120 min at a flow rate of 0.2 µl/min. The data acquisition
637 mode was set to obtain one high resolution MS scan in the FT part of the mass spectrometer at a
638 resolution of 60,000 full width at half-maximum (at m/z 400) followed by MS/MS scans in the
639 linear ion trap of the 20 most intense ions. The charged state screening modus was enabled to
640 exclude unassigned and singly charged ions and the dynamic exclusion duration was set to 30s.
641 The ion accumulation time was set to 300 ms (MS) and 50 ms (MS/MS).

642 For label-free quantification, the generated raw files were imported into the Progenesis LC-
643 MS software (Nonlinear Dynamics, Version 4.0) and analyzed using the default parameter
644 settings. MS/MS-data were exported directly from Progenesis LC-MS in mgf format and
645 searched against a decoy database the forward and reverse sequences of the predicted proteome
646 from *S. cerevisiae* (SGD, download date: 15/6/2012, total of 13,590 entries) using MASCOT
647 (version 2.4.0). The search criteria were set as follows: full tryptic specificity was required
648 (cleavage after lysine or arginine residues); 3 missed cleavages were allowed;
649 carbamidomethylation (C) was set as fixed modification; oxidation (M) as variable modification.
650 The mass tolerance was set to 10 ppm for precursor ions and 0.6 Da for fragment ions. Results
651 from the database search were imported into Progenesis and the final peptide feature list and the
652 protein list containing the summed peak areas of all identified peptides for each protein,
653 respectively, were exported from Progenesis LC-MS. Both lists were further statically analyzed
654 using an in-house developed R script (SafeQuant) and the peptide and protein false discovery
655 rate (FDR) was set to 1% using the number of reverse hits in the dataset [57].

656

657

658 *Transcriptomics*

659

660 *mRNA extraction*

661 For the extraction of mRNA from yeast, the RiboPure™ RNA Purification Kit, yeast
662 (Ambion®, Life Technologies/Thermo Fisher Scientific Co. Carlsbad, California, United States)
663 was used as described by the manufacturer. Frozen cell pellets of 3×10^7 cells were suspended in
664 the lysis mixture. Vortexing was done by using the The Ambion® Vortex Adapter (Ambion®,
665 Life Technologies/Thermo Fisher Scientific Co. Carlsbad, California, United States). The mRNA
666 was collected in 70 µl elution solution. The quality and yield of the RNA was checked with a
667 NanoDrop ND-1000 Spectrophotometer (Thermo Fisher Scientific, Waltham, MA USA). The
668 samples were stored as 5 µg mRNA aliquots at -80 °C. 1 µl of 1:10 diluted mixture of 92
669 polyadenylated non-yeast transcripts was added as a spike-in for sequencing quality control
670 (ERCC RNA Spike-In control mix, Life Technologies, Carlsbad, California, United States) [58].

671

672

673 *mRNA sequencing and mapping*

674 The mRNA was sequenced by ServiceXS (Leiden, The Netherlands). The quality and
675 integrity of the RNA-samples was determined with a Nanodrop ND1000 spectrophotometer and
676 analyzed on a RNA 6000 Lab-on-a-Chip using bioanalyzer (Agilent Technologies, Santa Clara,
677 CA, USA). The cDNA libraries were generated by using the Illumina TruSeq mRNA-Seq
678 Sample Prep Kit v2 (Illumina, San Diego, CA, USA). In short, mRNA was isolated from total
679 RNA using the oligo-dT-magnetic beads, fragmented and cDNA synthesis was performed. The
680 cDNA was ligated with the sequencing adapters and amplified by PCR. The quality of the
681 amplified cDNA was measured with a DNA 1000 Lab-on-a-Chip. The fragment sizes ranged
682 between 300 and 500 bp.

683 The cDNA was clustered in the flow cell of the sequencer by an Illumina cBot and the
684 sequencing was done on an Illumina HiSeq 2000. A cDNA concentration of 4.5 pM was used for
685 sequencing, in two reads of 100 cycles each, controlled by the HiSeq control software HCS
686 v2.0.12.0. Image analysis, base calling and quality checks were performed with the Illumina data
687 analysis pipeline RTA v1.13.48 and/or OLB v1.9 and CASAVA v1.8.2. All data consisted of
688 >0.9 Gb read depth and a quality Q30-score >80% per sample. One time point set, replicate 1 t10
689 (26.8hrs), was excluded by this criteria.

690 Reads were mapped to EF4 genome assembly using TopHat software v2.0.8 and gene
691 annotation from Ensembl release 71. Per gene expression values were calculated using
692 Cufflinks/Cuffdiff package v. 2.1.1. Data quality was assessed by principle component analysis
693 on the resulting raw data of spike-in controls, and of all gene profiles. Outliers resulting from
694 poor sequencing results in the spike-in (i.e., Figure 2-source data 2 Table S3.1, samples from
695 replicate 1: t2_M_Feb and t7_EW_Feb) or the full genome profiles (i.e., Figure 2-source data 2
696 Table S3.1, samples from replicate 2: t14_M_May, t14_D_May and t14_EW_May) were
697 removed. As a result 3 time points were omitted: replicate 1 t2 (1hr), replicate 1 t7 (14hrs),
698 replicate 2 t14 (53hrs)). In total, 4 time points were omitted.

699

700

701 Data processing

702

703 *Mathematical unmixing*

704 Mathematical unmixing rests on the idea that a system of linear equations can be solved
705 when (i) the number of equations is equal to the number of unknowns and (ii) these are
706 independent (see supplemental note 1 below for terminology, explanation, and validation of the
707 method). In our experiment this idea was implemented, for each time point, by means of a
708 weighted ‘unmixing’ matrix (**W**) whose rows represent the fractions of cell types (i.e. mothers,
709 dead, and daughter cells) in the harvested ‘mixed-cell samples’. The fractional composition of
710 each mixed-cell sample was acquired by using flow cytometry on dye stained cells, using PI and
711 AvF to assess the amount of live mother cells, dead cells, and daughter cells (see: Materials and
712 Methods, Flow cytometry analysis of sample composition, and see Figure 2-source data 1 Table
713 S2.f for each time point’s matrix).

714 For the mathematical unmixing validation experiments, the fractional compositions of the
715 mixed-cell samples were defined by mixing different pure cell sample types (i.e. log-phase,
716 deceleration-phase, and stationary-phase cells) in known ratios. Protein and mRNA abundance
717 values for the mixed-cell samples were measured by targeted (SRM) proteomics (for validation
718 only) and shotgun proteomics (for validation and aging cells), or RNA seq transcriptomics (for

719 validation and aging cells). Equation (3), present in the supplemental note 1 below, was
720 implemented using a custom R script for the actual unmixing procedure. Following the unmixing
721 of the data, should the resulting data contain “unsolvable” entries (see supplemental note 1
722 below), a data quality criteria was applied: at least five time points per time trace (0 hour – 72
723 hour) should be solvable, otherwise the protein or transcript was removed from the dataset. In
724 cases which passed this criteria but still contained one or more unsolvable entries in the time
725 series, the missing data was linearly interpolated by the time points neighboring the data in
726 question using the ‘approx’ interpolation function in R, implemented by the zoo package [59].
727 Datasets were subsequently normalized to one million for both the shotgun proteomes and
728 transcriptomes.

729

730 *Correction for effect of beads*

731 A simple correction step accommodating for the specific protein losses caused by the
732 presence of the beads was applied to the relevant data, and is explained in the supplemental note
733 2 below. The loss was specific for a protein, highly reproducible and independent of the ratio of
734 beads to cells (Figure 2–figure supplement 4). Briefly, a protein specific correction factor was
735 calculated for each protein of the proteome from the difference between a sample with and
736 without beads, averaged over 2 replicates. The correction was applied to the raw proteome
737 datasets, prior to mathematical unmixing, and on all samples that contained beads.

738

739 *Selection of the young time point reference sample*

740 A young time point to compare aged cells to was selected and processed as described in the
741 supplemental note 3 below. Briefly, the time series proteome and transcriptome data were
742 standardized to the difference between the starting time point (7.8 hour in the column) and an
743 unprocessed sample, and only data from 7.8 hour and later was considered in the analyses. This
744 was done to avoid mislabeling any biological recovery from the biotinylation and loading
745 procedure as being aging related and to maintain quantitative datasets for analysis.

746

747 *Data fitting and filtering*

748 For both the shotgun proteomes and transcriptomes, replicate datasets were fitted with a
749 LOESS polynomial regression using a standard span value of 0.75 [60], using the replicates of
750 unprocessed samples, and the replicate time series of 7.8 hour – 72 hour, as input for the
751 regression. Final datasets were generated by resampling the regression fit at each time point
752 physically sampled in the experiment (including those prior to 7.8 hour, for completeness and
753 consistency). Datasets are available in Table S2.5a and S3.5a for each of the proteome and
754 transcriptome supplementary Tables (Figure 2–source data 1 and 2). A noise threshold was
755 applied to the time series datasets using the coefficient of variation between replicates with a
756 cutoff of 0.3, corresponding to retention of 90.9% and 84.4% of the most reproducible data for
757 the proteome and transcriptome, respectively (Figure 2–figure supplement 6) (dataset available
758 in Figure 2–source data 3 and 4, Table S4 and S5). From this final dataset of 1494 proteins and
759 4904 transcripts, 2 proteins and 2 transcripts contained a negative data point in their time series
760 profiles, and were removed from both mother and daughter datasets in subsequent analyses.
761 Unless specified otherwise (see network methods), the final datasets used for analyses consisted
762 of the fitted regression data (Figure 2–source data 3 and 4, Table S4 and S5), from 7.8 hour of
763 cultivation and later.

764

765 *GO term selection and annotation*

766 Gene functional enrichments were determined by using the DAVID Bioinformatics
767 Resources version 6.7 [61]. Corresponding background gene lists of indicated size (Figure 3-
768 source data 1 Table S6) were used for each enrichment analysis. Annotation clusters determined
769 by DAVID (groupings of related genes based on the agreement of sharing similar annotation
770 terms) having an enrichment score of > 0.5 were selected for consideration, if a GO term was
771 enriched in the cluster with a p -value < 0.1 . For larger datasets, a more stringent enrichment
772 score cutoff of either > 0.9 or > 1.0 was used, as seen from lowest score cutoffs listed in the table
773 below per analysis. A representative naming for the enrichment was selected after evaluation of
774 the annotation cluster's GO terms (see Figure 3-source data 1 Table S6). Visualization of
775 representative terms in clouds was made using the R wordcloud package [62] using the
776 annotation cluster enrichment score as a size-scaling factor. If duplicate terms were present
777 within a GO term enrichment list, the higher enrichment was used for visualization purposes. In
778 one instance (the most responsive cluster of the proteome network) an unclear term ('BNR
779 repeat') representing 3 genes was omitted even though it passed our criteria for inclusion.

780

781 *Protein complex deregulation*

782 A curated list of protein complexes derived from the 'cellular component' gene ontology
783 was downloaded from yeastgenome.org [38]. Using the fold changes of gene products (i.e. either
784 proteins or transcripts) at any given time point within a protein complex of interest, the degree of
785 deregulation was assessed by measuring the interquartile of the distribution of the fold changes
786 of the complex's gene products.

787

788 *Network analysis*

789 To infer the high-level directional networks (Figure 6B, Figure 7-figure supplement 4B)
790 and find causal relations, six data analysis steps (Figure 6-figure supplement 1A) were
791 undertaken, as expanded upon below in the supplemental note 4. Briefly, these were: 1. Starting
792 from the replicate datasets, the gene expression time series of both the transcriptome and
793 proteome were filtered to remove flat and/or noisy profiles using the R package GPREGGE [63].
794 2. The gene product networks (i.e transcriptome or proteome) were generated, based on the gene
795 profiles of the respective time course data sets, using the R package GeneNet [35,64]. This
796 included generating an undirected network by calculating the partial correlation among gene
797 profiles (Figure 6-figure supplement 1B and C, Figure 7-figure supplement 4A). 3. Following
798 this, a directed network was generated from the undirected network, based on an assessment of a
799 gene profile's ability to predict another gene profile (Figure 6-figure supplement 1D and E,
800 Figure 7-figure supplement 4A) [35,64]. 4. The nodes in the network were clustered together,
801 using the method in [65] using the R package igraph (Figure 6A, Figure 7-figure supplement
802 4A) [34]. The causal in/out connections among genes were calculated for all the network clusters
803 and listed in a direction matrix (listed in Figure 6-source data 1 Table S7). 5. A high-level
804 directional network was generated, where the clusters are plotted in order of their causal ranking
805 by drawing the direction matrix as arrows between the clusters. 6. A sensitivity analysis was
806 made to determine the optimal sparsity of the networks and the cut-off for the partial correlation
807 among gene profiles.

808

809

810

811 **Figure legends:**

812

813 **Figure 1. Experimental design for analysis of molecular changes during the replicative**
814 **lifespan of yeast and its validation. (A)** Schematic overview of the column-based cultivation
815 and data analysis pipeline with 16 parallel columns, where (zoom in) mother cells (M)
816 containing streptavidin-bound (green triangles) iron beads (black circles) are captured on the
817 magnetized column and aged under constant environmental conditions, while the daughter cells
818 (D) are flushed away. Samples are collected in two replicate campaigns (R1, R2) at indicated
819 time points in the lifespan. **(B)** Flow-cytometry based assessment of viability of mother (Avidin-
820 FITC positive) and daughter (Avidin-FITC negative) cells in R1 and R2, calculated for each time
821 point comparing viable (PI negative) vs inviable (PI positive) cells in harvested samples Mix 1-3
822 (see figure 2A for explanation of Mix 1-3). Solid black line represents cell viability in time
823 measured for the same strain in the same media using a microfluidic device [21] (data from [18]
824 was obtained from the authors). **(C)** Cell size is qualitatively assessed with median forward
825 scatter of live mothers (Avidin-FITC positive, PI negative) vs live daughters (Avidin-FITC and
826 PI negative). Dashed line represents the median forward scatter of young cells that have reached
827 the fully-grown cell size to start their first division. **(D)** Aging is qualitatively assessed
828 throughout the experiment by observing an increase in median WGA intensity over time in a
829 population of primarily mothers (Mix 2) compared to a sample composed primarily of daughters
830 flushed out of the column (Mix 3). Inset: bright field (BF) and fluorescence microscopy image of
831 cell stained with AlexaFluor 633 conjugated wheat-germ agglutinin (WGA) which selectively
832 binds chitin in bud scars. Scale bar 5 μm .

833

834 **Figure 1–figure supplement 1. Setup of the aging columns.**

835 **Figure 1–figure supplement 2. Cellular aging under constant conditions.**

836 **Figure 1–figure supplement 3. Cell counts per timepoint.**

837 **Figure 1–figure supplement 4. Simulated yeast aging population dynamics.**

838 **Figure 1–figure supplement 5. Characterization of mixed-cell samples.**

839 **Figure 1-source data 1. Table S1: Materials used for construction of novel column-based**
840 **cultivation method.**

841

842 **Figure 2. Mathematical unmixing of proteomes and transcriptomes in mixed-cell**
843 **populations. (A)** For each time-point in the aging experiment three samples (mixed-cell samples
844 1,2,3; originating from different harvesting steps) and composed of different fractions of Mother
845 (M, green), Daughter (D, blue) and Dead cells (De, red) were harvested and analyzed. On the
846 basis of the compositions of the mixed-cell samples ($w_{M,D,De}$) and the determined proteome or
847 transcriptome data of the mixed-cell samples ($A_{\text{mix}1,2,3}$), with the mathematical unmixing we
848 obtained unmixed data ($A_{M,D,S}$) over the time course of 72 hours, from 2 replicates. See Figure 1-
849 figure supplement 5 for details about determining the composition of the mixed-cell samples and
850 Figure 2-figure supplement 3 for the un-mixing method. Data from proteome **(B)** and
851 transcriptome **(C)** replicates highly correlated (Spearman correlation > 0.85) for mother (circles)
852 and daughter cells (squares), indicating high reproducibility of the experimental and data
853 processing pipelines. **(D, E)** Levels of random chosen proteins **(D)** and transcripts **(E)** from both
854 replicate measurements (grey) and the fit (solid line) are indicated for unmixed mother data. Raw
855 abundance is a measure of MS peak intensities (proteome) or Fragments Per Kilobase of
856 transcript per Million mapped reads (FPKM) (transcriptome).

857

858
859 **Figure 2–figure supplement 1. Validation of the mathematical un-mixing procedure.**
860 **Figure 2–figure supplement 2. Validation of the mathematical un-mixing procedure,**
861 **shotgun proteome and RNA sequencing.**
862 **Figure 2–figure supplement 3. Generation and composition of the mixed-cell samples.**
863 **Figure 2–figure supplement 4. Validation of the bead effect correction.**
864 **Figure 2–figure supplement 5. Overview of the experimental pipeline.**
865 **Figure 2–figure supplement 6. Selection of genes with highest similarity between replicates.**
866 **Figure 2-source data 1. Table S2: The shotgun proteome data processing**
867 **Figure 2-source data 2. Table S3: The transcriptome data processing**
868 **Figure 2-source data 3. Table S4: The final shotgun proteome data**
869 **Figure 2-source data 4. Table S5: The final transcriptome data**

870
871 **Figure 3: The aging proteome. (A)** The Spearman correlation at progressive time points
872 compared to the young reference sample for the mother and daughter proteome shows a
873 divergence away from a youthful state for the mother. **(B)** The numbers of proteins changing by
874 at least two-fold from the reference (young) sample per time point. Blue and red bars and text
875 represent changes that had not occurred previously, either up or down regulated, respectively.
876 Grey bars and text are changes that already occurred at a previous time point. Gene functional
877 enrichments per grouped time points were derived from Gene Ontologies and are scaled with
878 significance of enrichment obtained by DAVID bioinformatics resource version 6.7 (scale bar,
879 DAVID enrichment score see Materials and methods and Table S6 (Figure 3-source data 1)).

880
881 **Figure 3–figure supplement 1. The aging transcriptome diverges minimally from a young**
882 **profile.**
883 **Figure 3–figure supplement 2. Changes in mother-age dependent daughter profiles.**
884 **Figure 3–figure supplement 3. Profiles that contribute to the enrichments of proteins**
885 **changing more than 2 fold.**
886 **Figure 3–figure supplement 4. Single protein profiles matching literature.**
887 **Figure 3-source data 1. Table S6: Full lists of GO-term enrichment scores for all**
888 **enrichment analyses.**

889
890 **Figure 4: Protein profiles in aging yeast. (A)** Expression profiles for the proteome were
891 clustered using the Ward clustering algorithm and plotted in a dendrogram. Visualization of most
892 prominent (red line in dendrogram) protein fold change profiles (log₂ scale) occurring with age,
893 showing up-regulated (cluster 1), down-regulated (cluster 2) and mainly flat (cluster 3) profiles.
894 Gene functional enrichments per grouped time points were summarized into representative terms
895 as in Figure 3B. **(B)** Unidirectional changes occurring with aging are illustrated with a heat map
896 of the fold changes (log₂ scale) of proteins in the aging mother compared to the young reference
897 sample.

898
899 **Figure 4–figure supplement 1. Comparison of aging proteomes and transcriptomes.**
900 **Figure 4–figure supplement 2. Analysis of two fold changes per time point in the aging**
901 **transcriptome.**
902 **Figure 4–figure supplement 3. Analysis of aging changes clustered by expression profile.**

903
904
905

906 **Figure 5: A post-transcriptional overrepresentation in protein biogenesis with aging.** (A) A
907 progressive uncoupling of the proteome from the transcriptome in time is apparent from the
908 decreasing Spearman correlation between the two. (B) Co-expression map showing fold changes
909 (\log_2) of 72h aged samples compared to the young reference, plotting the proteome versus the
910 transcriptome. Quadrants 1 and 3 (Q1 and Q3) represent changes where the protein changes
911 match their transcript changes (coupled), while quadrants 2 (Q2) and 4 (Q4) reflect opposite
912 changes (uncoupled). Summarizing terms per quadrant are derived from Gene Ontologies as in
913 Figure 3B (scale bar DAVID enrichment score).

914
915 **Figure 5–figure supplement 1. Correlation of proteome versus transcriptome using**
916 **alternative statistical methods for comparison.**

917 **Figure 5–figure supplement 2. Co-expression map showing fold changes of 10.7h, 22h, 45.4h**
918 **and 72.3h compared to the young reference, highlighting gene products contributing to**
919 **gene enrichments.**

920 **Figure 5–figure supplement 3. Change in posttranscriptional protein overabundance with**
921 **aging.**

922

923 **Figure 6: Network inference identifies protein biogenesis related genes as causal force**
924 **during aging.** (A) The directed and clustered transcriptome network consists of 3631 edges,
925 connecting 1241 nodes in 8 clusters (see Figure 6-figure supplement 1 and supplemental note 4
926 for further details). Only actual relations are depicted, the causal direction between two nodes is
927 indicated with an arrow, where the arrowhead points to the responsive node. (B) Clusters ranked
928 from more causal to more responsive in the causality network (from blue to red for clusters 1
929 through 8). The degree of causality is determined by the ratio of the outgoing over incoming
930 connections per cluster (from A). The blue to red arrows indicate the sum of outgoing arrows
931 between two clusters, where arrow thickness is logarithmically scaled to the number of arrows
932 (from A), i.e. the summed predictive power of one cluster over the other. Summarizing terms per
933 cluster are derived from Gene Ontologies as in Figure 3B (scale bar DAVID enrichment score).

934
935 **Figure 6–figure supplement 1. The transcriptome network.**

936 **Figure 6–figure supplement 2. Network cluster gene enrichments in the co-expression map.**

937 **Figure 6-source data 1. Table S7: The direction matrices and the sensitivity analyses for the**
938 **proteomic and transcriptomic high-level directional networks.**

939

940 **Figure 7: Loss of stoichiometry in protein complexes is a consequence during aging.** (A)
941 Illustrative representation of loss of stoichiometry within a protein complex (red, blue and green
942 squares) during aging. Changing levels of proteins may be coordinated (left) or uncoordinated
943 and result in a loss of complex stoichiometry (right). (B) Stoichiometry loss (for a single
944 complex defined as the InterQuartile Range (IQR) of the distribution of fold changes of the
945 components) is plotted for all complexes in proteome and transcriptome datasets as bean plots
946 during aging. The genes in common between the datasets are used. Thick horizontal line
947 represents the mean of the distribution of all complexes, thin colored lines the individual
948 complexes' stoichiometry loss, and the outline the distribution of all complexes. (C) Illustration
949 of the loss of stoichiometry of protein complexes during aging for the proteome (grey lines), with
950 specific examples highlighted (colored lines). (D) Illustration of the loss of protein stoichiometry
951 in proteasome (left panel) and the vacuolar proton transporting V-type ATPase, V1 domain (right

952 panel). The protein abundance changes (log₂-scale) of the complex' components are plotted in
953 time. The degree of stoichiometry loss is indicated with a box plot.

954
955 **Figure 7–figure supplement 1. Proteome data of distribution of changes within complexes in**
956 **the cell.**

957 **Figure 7–figure supplement 2. Transcriptome data of distribution of changes within**
958 **complexes in the cell.**

959 **Figure 7–figure supplement 3. Loss of stoichiometry occurring in the protein complexes.**

960 **Figure 7–figure supplement 4. The proteome network.**

961

962

963 **Supplemental figure legends:**

964

965

966 **Figure 1–figure supplement 1. Setup of the aging columns.** (A) Prior to being loaded on the
967 aging column, the yeast cells are labeled with membrane impermeable Sulfo-NHS-LC-Biotin
968 (step 1, green triangles). The LC-linker in Sulfo-NHS-LC-Biotin has a spacer arm length of 22.4
969 Å. The NHS-ester forms a covalent amide bond with primary amine groups in the Lysines and at
970 the N-termini of the yeast cell wall proteins. Streptavidin-coated magnetic beads (black circles,
971 step 2) bind with high affinity to the biotin-labeled cells. (B) The side view of one column set up.
972 Medium is pumped with a flow rate of 170 ml/h via air permeable silicone tubing (1) and a T-
973 connector (2) into the magnetized column holding the magnetic-bead-coupled yeast cells (3).
974 The medium leaves the magnetized column via the U-shaped tubing below the column (4), a T-
975 connector (5) and the outlet tubing (6) into a waste jar (7). The medium level in the column is
976 regulated with the air valve on top of the T-connector (2) in combination with the backpressure
977 caused by medium in the U-shaped tubing after the column (4). To disrupt the steady laminar
978 effluent flow, air was allowed to enter the system via T-connector (5). During incubation at the
979 columns, the flow was started and clamp 1 (C.I) and clamp 3 (C.III) are open, while the air valve
980 is closed (C.II). (C) The items used to build the setup are presented in a simplified 2D view and
981 listed in Figure 1-source data 1 Table S1. (D) 3D view of the magnet's stand with two magnets
982 present.

983 **Figure 1–figure supplement 2. Cellular aging under constant conditions.** The aging columns
984 maintain constant oxygen (A) and glucose (B) concentrations and pH (C) during cultivation.
985 Oxygen concentration was determined using the Optical Oxygen Meter Fibox 3 in both fresh
986 medium and the column effluent (A). Glucose concentration was determined by enzyme-based
987 assay Enzytec™ fluid D-Glucose (B). The pH of the medium was measured by a conventional
988 pH-meter in fresh medium (t = 0h) and in the column effluent after 24h and 48h in duplicate (C).
989 (D) Fluorescence microscopy image of AlexaFluor 633 conjugated wheat-germ agglutinin
990 (WGA) stained cells selectively staining chitin in bud scars. (E) Distribution of replicative ages
991 of (n) cells in samples harvested at different time points as determined by counting bud scars in
992 AlexaFluor 633-WGA labeled cells. The bud scars were counted double blind from confocal z-
993 stack images. (F) Numbers of cells per mixed-cell sample, per time point, and for each replicate.

994 **Figure 1-figure supplement 3. Cell counts per timepoint.** The cell counts present in each
995 mixed-cell sample harvested from each time point of the experiment. These values (along with

996 fractional compositions present in Figure 2-figure supplement 3B) were used to calculate the
997 weighted lifespan curve presented in Figure 1B.

998
999 **Figure 1-figure supplement 4. Simulated yeast aging population dynamics.** Due to
1000 biological cell-to-cell variation in cell division rates, the age distribution of a starting cohort of
1001 cells increases at later time points. This results in an increasing overlap of ages in the mother cell
1002 populations harvested at later time points, as modeled for a starting cohort of 1000 cells (see
1003 methods: *Harvesting time points*). The age is indicated as the replication life span (RLS). (A)
1004 shows the distribution of mother cell ages in samples harvested at indicated equally spaced time
1005 points, (B) shows the distribution when samples are harvested at exponentially spaced time
1006 points, minimizing the overlap of information between neighboring samples.

1007
1008 **Figure 1-figure supplement 5. Characterization of mixed-cell samples.** (A) Cells were
1009 stained with avidin conjugated FITC (AvF), which only labels cells coming from the initial
1010 biotin labeled cohort (see Figure 1-figure supplement 1A), and with propidium iodide (PI),
1011 which is permeable only to dead cells and fluoresces upon intercalation with DNA. (B)
1012 Analyzing the stained samples on a flow cytometer clearly distinguishes the populations of dead
1013 or alive mother cells and dead or alive daughter cells, based on fluorescence emission.
1014 Quantification of these populations gives the fractional compositions of each mixed-cell sample
1015 (Mix 1,2,3 in Figure 2-figure supplement 3) collected per time point. SSC-A is the FACS' side
1016 scatter area, FCS-A is the FACS' forward scatter area, FL1-A is the FITC fluorescence emission
1017 peak area, FL3-A is the PI fluorescence emission peak area.

1018
1019 **Figure 2-figure supplement 1. Validation of the mathematical un-mixing procedure.** (A)
1020 Schematic representation of samples used for validation of the mathematical un-mixing
1021 procedure, taken from fermenter-grown yeast. Log-phase represents mid-exponential growth of
1022 the culture (L), deceleration phase represents a decreased growth rate around the diauxic shift
1023 (D), and stationary phase is a nutrient deprived culture (S). Each phase of cultivation has a
1024 unique transcriptional and proteomic signature. (B) The abundance of 207 proteins was
1025 measured with targeted (SRM) proteomics in the samples L, D and S, and in three mixed cell
1026 samples composed of different ratios of L, D, and S. The protein abundance in the pure samples
1027 and the abundance derived after mathematical un-mixing of the data obtained from the mixed
1028 cell-sample is shown for 10 representative proteins of the 207 proteins. (C) As in B, for all 207
1029 proteins.

1030
1031 **Figure 2-figure supplement 2. Validation of the mathematical un-mixing procedure,**
1032 **shotgun proteome and RNA sequencing.** (A) As in Figure 2-figure supplement 1C but now for
1033 proteome data obtained by shotgun proteomics. The Pearson correlations are as high as 0.989,
1034 0.992, and 0.993, for Log, Deceleration, and Stationary phase samples, respectively, in the \log_2
1035 scale (top panels). Bottom panels show the relative errors for all proteins quantified; the
1036 abundance of the indicated number of proteins is recovered with less than 20% relative error. (B)
1037 As in (A) but here for the mRNA seq transcriptome data showing Pearson correlations of 0.945,
1038 0.956, and 0.801 for Log, Deceleration, and Stationary phase samples, respectively, in the \log_2
1039 scale (top panels). The indicated numbers of transcripts were recovered with less than 20%
1040 relative error (bottom panels). All abundances are plotted on a \log_2 -scale.

1041

1042 **Figure 2–figure supplement 3. Generation and composition of the mixed-cell samples.** (A) I:
1043 A cohort of cells with cell-wall attached beads is maintained in the magnetized column (magnet
1044 1) and harvested at set time points (column fraction) when also a fraction with mainly daughter
1045 cells is collected (column effluent, mix 3). II: The harvested column fraction was applied for
1046 further enrichment on “The Big Easy” EasySep™ Magnet (magnet 2). The bead labeled aged
1047 cells stay in the glass tube, while the non-bead labeled young cells are removed by pipetting.
1048 This wash is repeated 3 times, resulting in a sample enriched for mothers (mother enriched; mix
1049 2), and a wash fraction (wash, mix 1). The fractional population sizes of these three mixes,
1050 schematically represented in III, were determined (See Figure 1–figure supplement 5) before
1051 storage at -80°C . (B) The measured compositions of mother, daughters, and dead cells present in
1052 each mixed-cell sample harvested from each time point of the experiment. These fractional
1053 compositions were used in the mathematical un-mixing procedure. (C) Example of the
1054 mathematical unmixing procedure: Hsp104 protein abundances (MS peak intensity) for each
1055 time point in each of the mixed-cell samples (left panel) and the resulting unmixed abundances
1056 visualized as fold changes on a log₂-scale (right panel).

1057
1058 **Figure 2–figure supplement 4. Validation of the bead effect correction.** The effect of the
1059 beads on the proteome was highly reproducible, regardless of the number of beads per sample,
1060 and was unrelated to other biological stimuli applied on the cells. (A) Samples generated at
1061 different steps during biotinylation, bead labeling, and harvesting were assessed for their
1062 similarity to a sample which has undergone all processing steps (sample D), as would the starting
1063 (bead labeled) sample of the experiment. Using targeted (SRM) proteomics focusing on 74
1064 proteins known to be either strongly affected or not affected when comparing a processed to an
1065 unprocessed sample, we found that the presence of beads alone within a sample (sample G) was
1066 enough to match the starting bead-labeled sample (sample D). The process of bead labeling itself
1067 (sample ‘H’, where bead labeling conditions were mimicked) yielded proteomes that bared little
1068 resemblance to our bead-containing samples. (B) Cells and bead counts from flow cytometry. A
1069 cohort of 4.0×10^8 cells (pink bar, left) was labeled with beads, by adding a known number of
1070 beads (4.8×10^8 beads, pink bar, right). The number of beads attached to a biotinylated cell
1071 population (1.2×10^8) is the difference between free beads before (4.8×10^8 beads, pink bar, right)
1072 and after bead-labeling (3.6×10^8 cells, gray bar, right). The number of cells with at least one bead
1073 was counted after bead labeling and cell enrichment on a magnet (after bead labeling, 1.2×10^8 ,
1074 gray bar, left). This yields on average 1.1 beads/cell. (C) The number of free beads and beads
1075 attached to the cells was determined for each sample with flow cytometry. The ratio of bead to
1076 cells increased maximally two fold in both replicates, most likely due to the detachment of cells
1077 from beads while being cultivated in the aging columns. (D) To study the effect of a small
1078 increase in bead concentration per sample we mixed unprocessed cells with different numbers of
1079 beads and performed targeted (SRM) proteomics, using the same 74 proteins for assessment. The
1080 median of the measured peak intensities decreased with an increase of beads per sample,
1081 indicating a loss of proteins. (E) Nonetheless, we found that varying the amount of beads in the
1082 sample in the range relevant to the aging experiment, did not alter the degree to which the sample
1083 was changed by the presence of the beads. The Pearson correlation of these samples to the
1084 standard (1.06 beads/cell) was higher than the correlation between two replicates of the standard.
1085 We conclude that the bead effect is highly reproducible, and can be redressed with a correction
1086 factor specific to each protein (See Supplementary text).

1087

1088 **Figure 2–figure supplement 5. Overview of the experimental pipeline.** Detailed view of the
1089 experimental pipeline to depict number of samples collected and data processing steps. Up to 16
1090 columns could be run simultaneously (cartoon of red magnet with column) and harvested
1091 throughout the aging procedure (cartoon of lifespan curve, fraction surviving at each age). Time
1092 points were exponentially spaced, and covered by two partially overlapping replicate campaigns
1093 (R1 and R2, dots showing time points), of 14 and 8 time points, respectively. For each time
1094 point, either two or three samples were required for mathematical unmixing of the population,
1095 i.e. early time points (blue dots), contained mainly live mother and live daughter cells, without
1096 mortality in the population, and therefore required only two samples for the mathematical
1097 unmixing of 2 unknowns. While later time points (red dots), contained increasing levels of dead
1098 cells, and required three samples for the mathematical unmixing of 3 unknowns. Replicate 1
1099 consisted of an unprocessed sample, five time points requiring two samples for unmixing, and 9
1100 time points requiring three samples for unmixing, totaling 38 samples. Replicate 2 had in the
1101 same way 23 samples, and together the two replicates consisted of 61 samples, which were
1102 processed with shotgun proteomics and RNAseq transcriptomics. After ‘omics’ data was
1103 collected, a bead correction was applied to proteome data coming from samples containing beads
1104 (see methods), and quality assessment of sequencing data removed 4 sets of samples from the
1105 transcriptome (see methods). The subsequent 61 proteome samples and 50 transcriptome samples
1106 were used for mathematical unmixing, which resulted in mother-specific data for the proteome
1107 (R1, 15 time points, and R2, 9 time points) and transcriptome (R1, 12 time points, R2, 8 time
1108 points). Corresponding daughter specific data also resulted from the unmixing procedure (not
1109 depicted in schematic). Finally, a reference time point was selected (7.8 hours, see methods) and
1110 the replicate datasets were merged to produce a single time series, for each of the proteome and
1111 transcriptome, spanning 12 time points throughout the replicative lifespan of the cells.

1112
1113 **Figure 2–figure supplement 6. Selection of genes with highest similarity between replicates.**
1114 (A) The coefficient of variation was calculated between the replicate datasets for each gene-
1115 product profile and a cutoff of 0.3 was used to select the most reproducible expression profiles
1116 between replicates, consisting of ~90.9% of the proteome, and ~84.4% the transcriptome
1117 datasets. (B) Example of a gene profile having a coefficient of variation of 0.1 (top panels) and
1118 coefficient of variation of 0.3, which just failed the cutoff for being included in the dataset
1119 (bottom panels). Data shown for both proteome (left panels), and transcriptome (right panels),
1120 with each replicate measurement (grey) and the fit (colored line).

1121
1122 **Figure 3–figure supplement 1. The aging transcriptome diverges minimally from a young**
1123 **profile.** Similar to Figure 3A, but for transcriptome. The Spearman correlation of the
1124 transcriptomes of mother and daughter cells at different time point compared to that of a
1125 reference (young) time point sample.

1126
1127 **Figure 3–figure supplement 2. Changes in mother-age dependent daughter profiles.** Heat
1128 maps (with row clustering based on Euclidean distance) showing changes for daughter profiles
1129 of each mother-age dependent time point for both proteome (A) and transcriptome (B). Gene
1130 functional enrichments were determined using David version 6.7 and summarized into
1131 representative terms (see methods section for details). The enrichment score provided by David
1132 for the summarized terms were used as a size-scaling factor for the text, with larger words being
1133 more significantly enriched (scale bar DAVID enrichment score). Enriched terms are shown next

1134 to each respective heat map, for genes changing by at least two-fold when comparing the
1135 daughter coming from the oldest mother age, to the daughter coming from the youngest mother
1136 age. This resulted in 33 genes 2 fold upregulated and 40 genes 2 fold down regulated in the
1137 proteome of 1494 proteins, and 31 genes upregulated and 190 genes down regulated in the
1138 transcriptome of 4904 transcripts. Fold changes are plotted on a log₂ scale.

1139

1140 **Figure 3–figure supplement 3. Profiles that contribute to the enrichments of proteins**
1141 **changing more than 2 fold.** Proteins contributing to the enrichment score for
1142 ‘stress.response.(General)’, or ‘glycolysis/gluconeogenesis’ that were increasing more than two
1143 fold with age, or proteins contributing to the enrichment score for ‘mitochondria.(general)’ and
1144 ‘DNA.replication’ that were decreasing more than two fold with age were selected for
1145 visualization (from Figure 3B). The fold changes are plotted on a log₂ scale.

1146

1147 **Figure 3–figure supplement 4. Single protein profiles matching literature.** Assessing the
1148 protein dynamics on the single cell level that were reported in the literature to occur in aging
1149 yeast shows agreement with our global-scale proteome dataset. Specifically, we see protein
1150 levels of the stress related chaperone Hsp104 and the translation elongation factor Tef1 to
1151 increase with aging as was shown using a microfluidic platform tracking single cells [29]. Using
1152 another microfluidic platform and GFP-tagged Vph1 protein as a marker for the vacuole, it was
1153 found that the vacuole increased in size more rapidly than the cell itself, suggesting a net
1154 increase of Vph1 protein levels to occur in the aging cell [21]. Our data shows Vph1 levels to
1155 increase with aging, in line with these observations. Furthermore, our proteome also captures the
1156 subtle changes described to occur with the Tpo1 protein and aging, where a computational model
1157 based on production and inheritance of the protein throughout aging predicted Tpo1 levels to
1158 initially increase and to then gradually decrease with age [32]. A recent study looking at protein
1159 abundances in young and old whole-cell extracts found that levels of the nucleoporins Nup116
1160 and Nsp1 decrease with age, while Nup100 and Nup53 did not change significantly [30], and for
1161 one other nucleoporin, Nup170, was shown that the levels increase with aging [31], which we all
1162 also detect in our proteome data (Figure 7D). Three proteins whose overexpression results in
1163 extended lifespan in yeast, Ras2 [33], Mxr1 [15], and Vma1 [28] were observed to decrease with
1164 age. Literature references are according to main text reference numbering.

1165

1166 **Figure 4–figure supplement 1. Comparison of aging proteomes and transcriptomes. (A)**
1167 Heat maps (with row dendrograms based on Euclidean distance) of proteome (top panel) and
1168 transcriptome (bottom panel) time series data, plotted as fold changes on a log₂ scale. **(B)** The
1169 raw abundances (log₂ scale) for the proteome and transcriptome are plotted against one another
1170 for young (left panel, age 7.8 hours) and old (right panel age 72 hours) cells.

1171

1172 **Figure 4–figure supplement 2. Analysis of two fold changes per time point in the aging**
1173 **transcriptome. (A)** The numbers of transcripts changing by at least two-fold from the reference
1174 (young) sample per time point. Red and blue bars or text represent changes that had not occurred
1175 previously, either up or down regulated, respectively. Grey bars or text are changes that already
1176 occurred at a previous time point. Gene functional enrichments per grouped time points were
1177 derived from Gene Ontologies and are scaled with significance of enrichment obtained by David
1178 version 6.7 (scale bar DAVID enrichment score). **(B)** Profiles that contribute to the enrichments
1179 of transcript changing more than 2 fold. Transcripts contributing to the enrichment score for

1180 ‘integral.to.membrane’, or ‘sporulation’ that increased more than two fold with age, or
1181 transcripts contributing to the enrichment score for ‘mitochondria.(respiration)’ and
1182 ‘mitochondria.(translation)’ that decreased more than two fold with age were selected for
1183 visualization (from A). The fold changes are plotted on a log₂ scale.

1184

1185 **Figure 4–figure supplement 3. Analysis of aging changes clustered by expression profile.**
1186 (A) Expression profiles for the transcriptome were clustered using the Ward clustering algorithm
1187 and plotted in a dendrogram. Three expression profile groups were selected for characterization
1188 (red vertical line). (B) The three most prominent profile expression clusters for the transcriptome
1189 (left three panels), showing mainly down-regulated (cluster 1 and 2) and up-regulated (cluster 3)
1190 profiles, and their average signature plotted relative to one another (right panel). Gene functional
1191 enrichments per grouped time points were summarized into representative terms as in Figure 3B.
1192 In one case (asterix, ‘translation regulation’), the enrichment value was scaled down (from 10.2)
1193 to the score of the next most enriched term (5.0), for better legibility of the other terms (with first
1194 three letters kept on the original scale). Transcript fold changes are plotted on a log₂ scale.

1195

1196 **Figure 5–figure supplement 1. Correlation of proteome versus transcriptome using**
1197 **alternative statistical methods for comparison.** Comparison of the proteome versus the
1198 transcriptome using the dataset of genes in common between the two. Using Pearson correlation
1199 on the raw data, Pearson correlation on log₂ transformed data, or Spearman or Kendall
1200 correlations on the raw data, show similar results: a decreasing correlation of the proteome and
1201 transcriptome with age.

1202

1203 **Figure 5–figure supplement 2. Co-expression map showing fold changes of 10.7h, 22h,**
1204 **45.4h and 72.3h compared to the young reference, highlighting gene products contributing**
1205 **to gene enrichments.** Co-expression map as in Figure 5B, showing fold changes of proteins and
1206 transcripts at 10.7h, 22h, 45.4h, and 72.3h aged time points compared to the young (7.8h)
1207 reference sample. Genes contributing to enrichment scores of the most enriched processes per
1208 quadrant at 72.3h of aging (sterol.biosynthesis from Q1, translation.regulation from Q2,
1209 cortical.actin.cytoskeleton from Q3, and endoplasmic.reticulum from Q4) are shown highlighted
1210 for each timepoint to illustrate their changes. The fold changes are plotted on a log₂ scale.

1211

1212 **Figure 5–figure supplement 3. Change in posttranscriptional protein overabundance with**
1213 **aging.** The fold change in abundance of a protein compared to a reference (young) sample,
1214 minus the fold change of its transcript, gives a quantity for its relative overabundance. Plotted in
1215 time are the summed values for the gene products per quadrant of the co-expression map in
1216 Figure 5B (grey points), and for all genes of the entire plot summed (black points). This shows a
1217 net increase over time of total relative protein overabundance, and a distinct behavior per
1218 quadrant.

1219

1220 **Figure 6–figure supplement 1. The transcriptome network.** (A) Cartoon illustrating the
1221 pipeline of the network analysis procedure, to go stepwise from gene expression time series (i.e.
1222 a gene profile) towards a high-level causal network. First, only nodes that have related gene
1223 profiles (based on partial correlations), as distinguished from all indirectly related gene profiles
1224 (based on simple correlations), are connected in the network (see B below). Second, the
1225 directionality of the arrows between two nodes was found by accounting for the relative

1226 reduction in the variability between the nodes. This revealed a causal relationship (see **D** below).
1227 Third, highly interconnected nodes were clustered. Finally, based on the clusters and the average
1228 directionality among the clusters, a high-level directional network was generated. For further
1229 details regarding these steps see supplemental note 4. (**B**) A simulated example to highlight the
1230 first step in (**A**), showing that the edge between nodes in the network depends on the partial
1231 correlation between the gene profiles. Two transcript profiles ('y' and 'z') were based on a
1232 computationally generated transcript profile ('x'), forming a small artificial network with edges
1233 between the nodes x and y in addition to x and z. While the simple correlations between all
1234 profiles are high (>0.995), the partial correlations are only high for x with y and x with z (grey
1235 dashed lines). Therefore, actual relations were only found from x to z and x to y (black edge).
1236 We can thus retrieve the true network, by making use of the partial correlations. (**C**) The
1237 undirected network for the transcriptome data. The edges between the nodes indicate only actual
1238 relations (based on partial correlations) between transcript profiles. All edges connected without
1239 partial correlations or nodes linked to the dataset without a partial correlation are omitted in this
1240 network. (**D**) An example to highlight the second step in (**A**) that the directionality between two
1241 transcript profiles was found by multiple testing of the standardized partial variances of the
1242 nodes. The standardized partial variances is the variances once the effect of the related profiles
1243 has been removed by regression analysis. For each of the connected node pairs (e.g. 'm' and 'n'),
1244 the direction goes from the profile with the highest standardized partial variance to the lowest.
1245 Basically, for a profile with a lower standardized partial variance, much of its variability is
1246 explained by the profiles connected to it, while for a profile with a high standardized partial
1247 variance, less of its variability is explained by the profiles associated to it. The latter profile has
1248 thus a higher ability to predict the first one than vice versa, and makes a profile with high
1249 standardized variance causal over a profile with a low standardized variance. The directionality
1250 is indicated as an arrow between the nodes. (**E**) The directed network for the transcriptome data.
1251 The arrowhead is pointing to the responsive node. For the clustered directed network see Figure
1252 6A and for the high level directional network see Figure 6B.

1253
1254 **Figure 6–figure supplement 2. Network cluster gene enrichments in the co-expression map.**
1255 (**A**) The genes represented in cluster 1 of the transcriptome networks (blue dots) were mapped on
1256 the co-expression map (grey dots; Figure 5B). The percentage of the genes enriched in each of
1257 the four Quadrants (Q1-4) is indicated, fold changes are plotted on a \log_2 scale (**B**) p -values for
1258 the enrichment of the genes in each cluster of the network in the four quadrants; transcriptome
1259 (top) and proteome (bottom). (**C**) The p -value for the enrichment of genes in each cluster in Q1
1260 and Q3 together representing a 'coupled' change in protein and transcript levels (left panel), and
1261 in quadrant Q2 and Q4 (uncoupled change) (right panel). A shift towards an uncoupled
1262 phenotype in the 'later' network clusters is apparent. The p -values are plotted on a \log_{10} scale.

1263
1264 **Figure 7–figure supplement 1. Proteome data of distribution of changes within complexes**
1265 **in the cell.** A curated list of protein complexes derived from the 'cellular component' gene
1266 ontology was downloaded from yeastgenome.org, and the horizontal box plots show the
1267 distribution of fold changes (\log_2 scale) occurring in the complex when comparing proteome
1268 data of the old (72 hours) sample to the young reference sample. Box-and-whisker plots are
1269 presented as follows: The thick black line within the box is the median of the data, the box
1270 extends to the upper and lower quartile of the dataset (i.e. to include 25% of the data above and

1271 below the median, respectively), whiskers (dashed lines) represent up to 1.5 times the upper or
1272 lower quartiles and circles represent outliers.

1273

1274 **Figure 7–figure supplement 2. Transcriptome data of distribution of changes within**
1275 **complexes in the cell.** Same as Figure 7–figure supplement 1 but for the transcriptome data.

1276

1277 **Figure 7–figure supplement 3. Loss of stoichiometry occurring in the protein complexes.**

1278 (A) Comparison between mother cells and mother-age dependent daughter cells, loss of
1279 stoichiometry within complexes. Bean plots showing the distribution of the loss of stoichiometry
1280 for all complexes in the cell (same as in Figure 7B), at each time point throughout aging. Mother
1281 and daughter cells plotted side by side, for the proteomes (left panel) and transcriptomes (right
1282 panel), showing that the mother cells’ proteome undergoes a greater degree of loss of
1283 stoichiometry within complexes than do mother-age dependent daughter cells. Stoichiometry
1284 loss for a single complex is calculated as the interquartile of the distribution of fold changes
1285 within the complex at any given time (i.e. the ‘box’ in Figure 7–figure supplement 1 and 2).
1286 Bean plots are drawn as follows: Thick horizontal line represents the mean of the distribution of
1287 all complexes, thin colored lines the individual complexes’ stoichiometry loss, and the outline
1288 the distribution of all complexes. (B) Illustration of the loss of protein stoichiometry in the
1289 vacuolar proton transportin V-type ATPase, V1 domain. The protein abundance changes (log2-
1290 scale) of the complex’ components are plotted in time. The degree of stoichiometry loss is
1291 indicated with a box plot.

1292

1293 **Figure 7–figure supplement 4. The proteome network.** (A) Undirected, directed, and
1294 clustered directed networks for the proteome dataset. The clustered directed network consists of
1295 669 edges, connecting 493 nodes in 5 clusters. (B) These interactions are summarized in a causal
1296 network: Clusters are ranked from more causal to more responsive (from blue to red for clusters
1297 1 through 5, placed on a turquoise arrow that depicts ranking) in the causality network. The
1298 degree of causality is determined by the ratio of the causal outgoing over incoming connections
1299 per cluster (from A). The blue to red arrows indicate the sum of outgoing arrows between two
1300 clusters (from A), i.e. the summed predictive power of one cluster over the other. Summarizing
1301 terms per cluster are derived from Gene Ontologies as in Figure 3B (scale bar DAVID
1302 enrichment score).

1303

1304

1305

1306

References:

- 1307 [1] T. Niccoli, L. Partridge, Ageing as a risk factor for disease, *Curr. Biol.* 22 (2012).
1308 doi:10.1016/j.cub.2012.07.024.
- 1309 [2] J.P. de Magalhães, D. Wuttke, S.H. Wood, M. Plank, C. Vora, Genome-environment
1310 interactions that modulate aging: powerful targets for drug discovery., *Pharmacol. Rev.* 64
1311 (2012) 88–101. doi:10.1124/pr.110.004499.
- 1312 [3] P.B. Medawar, An Unsolved Problem of Biology, *Evol. Heal. Dis.* (1952) 24.

- 1313 [4] M. A. McCormick, B. K. Kennedy, Genome-Scale Studies of Aging: Challenges and
1314 Opportunities, *Curr. Genomics*. 13 (2012) 500–507. doi:10.2174/138920212803251454.
- 1315 [5] B.K. Kennedy, M. Kaeberlein, Hot topics in aging research: Protein translation, 2009,
1316 *Aging Cell*. 8 (2009) 617–623. doi:10.1111/j.1474-9726.2009.00522.x.
- 1317 [6] A.E. Webb, A. Brunet, FOXO transcription factors: Key regulators of cellular quality
1318 control, *Trends Biochem. Sci.* 39 (2014) 159–169. doi:10.1016/j.tibs.2014.02.003.
- 1319 [7] M. Lagouge, N.-G. Larsson, The role of mitochondrial DNA mutations and free radicals
1320 in disease and ageing., *J. Intern. Med.* 273 (2013) 529–43. doi:10.1111/joim.12055.
- 1321 [8] N. Barzilai, D.M. Huffman, R.H. Muzumdar, A. Bartke, The critical role of metabolic
1322 pathways in aging, *Diabetes*. 61 (2012) 1315–1322. doi:10.2337/db11-1300.
- 1323 [9] R.K. Mortimer, J.R. Johnston, Life span of individual yeast cells., *Nature*. 183 (1959)
1324 1751–1752. doi:10.1038/1831751a0.
- 1325 [10] B.M. Wasko, M. Kaeberlein, Yeast replicative aging: a paradigm for defining conserved
1326 longevity interventions, 14 (2014) 148–159. doi:10.1111/1567-1364.12104.
- 1327 [11] A. Denoth-Lippuner, T. Julou, Y. Barral, Budding yeast as a model organism to study the
1328 effects of age, *FEMS Microbiol. Rev.* 38 (2014) 300–325. doi:10.1111/1574-6976.12060.
- 1329 [12] N.K. Egilmez, J.B. Chen, S.M. Jazwinski, Specific alterations in transcript prevalence
1330 during the yeast life span, *J. Biol. Chem.* 264 (1989) 14312–14317.
- 1331 [13] S.S. Lin, J.K. Manchester, J.I. Gordon, Enhanced Gluconeogenesis and Increased Energy
1332 Storage as Hallmarks of Aging in *Saccharomyces cerevisiae*, *J. Biol. Chem.* 276 (2001)
1333 36000–36007. doi:10.1074/jbc.M103509200.
- 1334 [14] I. Lesur, J.L. Campbell, The transcriptome of prematurely aging yeast cells is similar to
1335 that of telomerase-deficient cells., *Mol. Biol. Cell.* 15 (2004) 1297–1312.
1336 doi:10.1091/mbc.E03-10-0742.
- 1337 [15] A. Koc, A.P. Gasch, J.C. Rutherford, H.-Y. Kim, V.N. Gladyshev, Methionine sulfoxide
1338 reductase regulation of yeast lifespan reveals reactive oxygen species-dependent and -
1339 independent components of aging., *Proc. Natl. Acad. Sci. U. S. A.* 101 (2004) 7999–8004.
1340 doi:10.1073/pnas.0307929101.
- 1341 [16] G. Yiu, A. McCord, A. Wise, R. Jindal, J. Hardee, A. Kuo, et al., Pathways change in
1342 expression during replicative aging in *Saccharomyces cerevisiae*., *J. Gerontol. A. Biol.*
1343 *Sci. Med. Sci.* 63 (2008) 21–34. doi:63/1/21 [pii].

- 1344 [17] T. Smeal, J. Claus, B. Kennedy, F. Cole, L. Guarente, Loss of transcriptional silencing
1345 causes sterility in old mother cells of *S. cerevisiae*, *Cell*. 84 (1996) 633–642.
1346 doi:10.1016/S0092-8674(00)81038-7.
- 1347 [18] D.H.E.W. Huberts, J. González, S.S. Lee, A. Litsios, G. Hubmann, E.C. Wit, et al.,
1348 Calorie restriction does not elicit a robust extension of replicative lifespan in
1349 *Saccharomyces cerevisiae*., *Proc. Natl. Acad. Sci. U. S. A.* 111 (2014) 11727–11731.
1350 doi:10.1073/pnas.1410024111.
- 1351 [19] N.K. Egilmez, J.B. Chen, S.M. Jazwinski, Preparation and partial characterization of old
1352 yeast cells., *J. Gerontol.* 45 (1990) B9–B17. doi:10.1093/geronj/45.1.B9.
- 1353 [20] C.D. Powell, D.E. Quain, K.A. Smart, Chitin scar breaks in aged *Saccharomyces*
1354 *cerevisiae*, *Microbiology*. 149 (2003) 3129–3137. doi:10.1099/mic.0.25940-0.
- 1355 [21] S.S. Lee, I.A. Vizcarra, D.H.E.W. Huberts, L.P. Lee, M. Heinemann, Whole lifespan
1356 microscopic observation of budding yeast aging through a microfluidic dissection
1357 platform, *Proc. Natl. Acad. Sci.* 109 (2012) 4916–4920. doi:10.1073/pnas.1113505109.
- 1358 [22] G.E. Janssens, A.C. Meinema, J. González, J.C. Wolters, A. Schmidt, V. Guryev, et al.,
1359 Proteome data acquired during replicative aging of *S. cerevisiae*, (2015).
1360 doi:10.6019/PXD001714.
- 1361 [23] G.E. Janssens, A.C. Meinema, J. González, J.C. Wolters, A. Schmidt, V. Guryev, et al.,
1362 Transcriptome data acquired during replicative aging of *S. cerevisiae*, (2015) EBI
1363 ArrayExpress accession E–MTAB–3605.
- 1364 [24] B.K. Kennedy, N.R. Austriaco, L. Guarente, Daughter cells of *Saccharomyces cerevisiae*
1365 from old mothers display a reduced life span, *J. Cell Biol.* 127 (1994) 1985–1993.
1366 doi:10.1083/jcb.127.6.1985.
- 1367 [25] S.F. Levy, N. Ziv, M.L. Siegal, Bet hedging in yeast by heterogeneous, age-correlated
1368 expression of a stress protectant, *PLoS Biol.* 10 (2012). doi:10.1371/journal.pbio.1001325.
- 1369 [26] N. Erjavec, L. Larsson, J. Grantham, T. Nyström, Accelerated aging and failure to
1370 segregate damaged proteins in Sir2 mutants can be suppressed by overproducing the
1371 protein aggregation-remodeling factor Hsp104p, *Genes Dev.* 21 (2007) 2410–2421.
1372 doi:10.1101/gad.439307.
- 1373 [27] M.M. Crane, I.B.N. Clark, E. Bakker, S. Smith, P.S. Swain, A microfluidic system for
1374 studying ageing and dynamic single-cell responses in budding yeast, *PLoS One.* 9 (2014)
1375 1–10. doi:10.1371/journal.pone.0100042.
- 1376 [28] A.L. Hughes, D.E. Gottschling, An early age increase in vacuolar pH limits mitochondrial
1377 function and lifespan in yeast., *Nature.* 492 (2012) 261–5. doi:10.1038/nature11654.

- 1378 [29] Y. Zhang, C. Luo, K. Zou, Z. Xie, O. Brandman, Q. Ouyang, et al., Single Cell Analysis
1379 of Yeast Replicative Aging Using a New Generation of Microfluidic Device, *PLoS One*. 7
1380 (2012). doi:10.1371/journal.pone.0048275.
- 1381 [30] C.L. Lord, B.L. Timney, M.P. Rout, S.R. Wentz, Altering nuclear pore complex function
1382 impacts longevity and mitochondrial function in *S. cerevisiae*, *J. Cell Biol.* 208 (2015)
1383 729–744. doi:10.1083/jcb.201412024.
- 1384 [31] A. Denoth-Lippuner, M.K. Krzyzanowski, C. Stober, Y. Barral, Role of SAGA in the
1385 asymmetric segregation of DNA circles during yeast ageing, *Elife*. 3 (2014) 1–33.
1386 doi:10.7554/eLife.03790.
- 1387 [32] A. Eldakak, G. Rancati, B. Rubinstein, P. Paul, V. Conaway, R. Li, Asymmetrically
1388 inherited multidrug resistance transporters are recessive determinants in cellular
1389 replicative ageing., *Nat. Cell Biol.* 12 (2010) 799–805. doi:10.1038/ncb2085.
- 1390 [33] J. Sun, S.P. Kale, A.M. Childress, C. Pinswasdi, S.M. Jazwinski, Divergent roles of RAS1
1391 and RAS2 in yeast longevity, *J. Biol. Chem.* 269 (1994) 18638–18645.
- 1392 [34] G. Csárdi, A. Franks, D.S. Choi, E.M. Airoidi, D.A. Drummond, Accounting for
1393 Experimental Noise Reveals That mRNA Levels , Amplified by Post- Transcriptional
1394 Processes , Largely Determine Steady-State Protein Levels in Yeast, (2015) 1–32.
1395 doi:10.5061/dryad.rg367.
- 1396 [35] R. Opgen-Rhein, K. Strimmer, From correlation to causation networks: a simple
1397 approximate learning algorithm and its application to high-dimensional plant gene
1398 expression data., *BMC Syst. Biol.* 1 (2007) 37. doi:10.1186/1752-0509-1-37.
- 1399 [36] G. Csardi, T. Nepusz, The igraph software package for complex network research,
1400 *InterJournal. Complex Sy* (2006) 1695. doi:citeulike-article-id:3443126.
- 1401 [37] D.H.E.W. Huberts, B. Niebel, M. Heinemann, A flux-sensing mechanism could regulate
1402 the switch between respiration and fermentation, *FEMS Yeast Res.* 12 (2012) 118–128.
1403 doi:10.1111/j.1567-1364.2011.00767.x.
- 1404 [38] J.M. Cherry, E.L. Hong, C. Amundsen, R. Balakrishnan, G. Binkley, E.T. Chan, et al.,
1405 *Saccharomyces Genome Database: The genomics resource of budding yeast*, *Nucleic*
1406 *Acids Res.* 40 (2012). doi:10.1093/nar/gkr1029.
- 1407 [39] N.T. Ingolia, S. Ghaemmaghami, J.R.S. Newman, J.S. Weissman, Genome-wide analysis
1408 in vivo of translation with nucleotide resolution using ribosome profiling., *Science*. 324
1409 (2009) 218–223. doi:10.1126/science.1168978.
- 1410 [40] A. Belle, A. Tanay, L. Bitincka, R. Shamir, E.K. O’Shea, Quantification of protein half-
1411 lives in the budding yeast proteome., *Proc. Natl. Acad. Sci. U. S. A.* 103 (2006) 13004–
1412 13009. doi:10.1073/pnas.0605420103.

- 1413 [41] P. Laun, A. Pichova, F. Madeo, J. Fuchs, A. Ellinger, S. Kohlwein, et al., Aged mother
1414 cells of *Saccharomyces cerevisiae* show markers of oxidative stress and apoptosis, *Mol.*
1415 *Microbiol.* 39 (2001) 1166–1173. doi:10.1046/j.1365-2958.2001.02317.x.
- 1416 [42] Z. Hu, K. Chen, Z. Xia, M. Chavez, S. Pal, J.H. Seol, et al., Nucleosome loss leads to
1417 global transcriptional up-regulation and genomic instability during yeast aging, *Genes*
1418 *Dev.* 28 (2014) 396–408. doi:10.1101/gad.233221.113.
- 1419 [43] S.C. Johnson, P.S. Rabinovitch, M. Kaeberlein, mTOR is a key modulator of ageing and
1420 age-related disease., *Nature.* 493 (2013) 338–45. doi:10.1038/nature11861.
- 1421 [44] A.M. Cuervo, Autophagy and aging: keeping that old broom working, *Trends Genet.* 24
1422 (2008) 604–612. doi:10.1016/j.tig.2008.10.002.
- 1423 [45] P. Fabrizio, F. Pozza, S.D. Pletcher, C.M. Gendron, V.D. Longo, Regulation of longevity
1424 and stress resistance by Sch9 in yeast., *Science.* 292 (2001) 288–290.
1425 doi:10.1126/science.1059497.
- 1426 [46] M. Kaeberlein, R.W. Powers, K.K. Steffen, E.A. Westman, D. Hu, N. Dang, et al.,
1427 Regulation of yeast replicative life span by TOR and Sch9 in response to nutrients.,
1428 *Science.* 310 (2005) 1193–1196. doi:10.1126/science.1115535.
- 1429 [47] T. Vellai, K. Takacs-Vellai, Y. Zhang, A.L. Kovacs, L. Orosz, F. Müller, *Genetics:*
1430 *influence of TOR kinase on lifespan in C. elegans.*, *Nature.* 426 (2003) 620.
1431 doi:10.1038/426620a.
- 1432 [48] K.Z. Pan, J.E. Palter, A.N. Rogers, A. Olsen, D. Chen, G.J. Lithgow, et al., Inhibition of
1433 mRNA translation extends lifespan in *Caenorhabditis elegans*, *Aging Cell.* 6 (2007) 111–
1434 119. doi:10.1111/j.1474-9726.2006.00266.x.
- 1435 [49] P. Kapahi, B.M. Zid, T. Harper, D. Koslover, V. Sapin, S. Benzer, Regulation of lifespan
1436 in *Drosophila* by modulation of genes in the TOR signaling pathway, *Curr. Biol.* 14
1437 (2004) 885–890. doi:10.1016/j.cub.2004.03.059.
- 1438 [50] D.W. Lamming, L. Ye, P. Katajisto, M.D. Goncalves, M. Saitoh, D.M. Stevens, et al.,
1439 Rapamycin-Induced Insulin Resistance Is Mediated by mTORC2 Loss and Uncoupled
1440 from Longevity, *Science* (80-.). 335 (2012) 1638–1643. doi:10.1126/science.1215135.
- 1441 [51] C. Selman, J.M.A. Tullet, D. Wieser, E. Irvine, S.J. Lingard, A.I. Choudhury, et al.,
1442 Ribosomal protein S6 kinase 1 signaling regulates mammalian life span., *Science.* 326
1443 (2009) 140–144. doi:10.1126/science.1177221.
- 1444 [52] K.K. Steffen, V.L. MacKay, E.O. Kerr, M. Tsuchiya, D. Hu, L.A. Fox, et al., Yeast Life
1445 Span Extension by Depletion of 60S Ribosomal Subunits Is Mediated by Gcn4, *Cell.* 133
1446 (2008) 292–302. doi:10.1016/j.cell.2008.02.037.

- 1447 [53] M. Hansen, S. Taubert, D. Crawford, N. Libina, S.J. Lee, C. Kenyon, Lifespan extension
1448 by conditions that inhibit translation in *Caenorhabditis elegans*, *Aging Cell*. 6 (2007) 95–
1449 110. doi:10.1111/j.1474-9726.2006.00267.x.
- 1450 [54] A.B. Canelas, N. Harrison, A. Fazio, J. Zhang, J.-P. Pitkänen, J. van den Brink, et al.,
1451 Integrated multilaboratory systems biology reveals differences in protein metabolism
1452 between two reference yeast strains., *Nat. Commun*. 1 (2010) 145.
1453 doi:10.1038/ncomms1150.
- 1454 [55] C. Verduyn, E. Postma, W.A. Scheffers, J.P. Van Dijken, Effect of benzoic acid on
1455 metabolic fluxes in yeasts: A continuous-culture study on the regulation of respiration and
1456 alcoholic fermentation, *Yeast*. 8 (1992) 501–517. doi:10.1002/yea.320080703.
- 1457 [56] B. MacLean, D.M. Tomazela, N. Shulman, M. Chambers, G.L. Finney, B. Frewen, et al.,
1458 Skyline: An open source document editor for creating and analyzing targeted proteomics
1459 experiments, *Bioinformatics*. 26 (2010) 966–968. doi:10.1093/bioinformatics/btq054.
- 1460 [57] T. Glatter, C. Ludwig, E. Ahrné, R. Aebersold, A.J.R. Heck, A. Schmidt, Large-scale
1461 quantitative assessment of different in-solution protein digestion protocols reveals
1462 superior cleavage efficiency of tandem Lys-C/trypsin proteolysis over trypsin digestion, *J.*
1463 *Proteome Res*. 11 (2012) 5145–5156. doi:10.1021/pr300273g.
- 1464 [58] External-RNA-Controls-Consortium, Proposed methods for testing and selecting the
1465 ERCC external RNA controls., *BMC Genomics*. 6 (2005) 150. doi:10.1186/1471-2164-6-
1466 150.
- 1467 [59] A. Zeileis, G. Grothendieck, ZOO: S3 Infrastructure for Regular and Irregular Time
1468 Series, *J. Stat. Softw*. 14 (2005) 1–27.
- 1469 [60] R. Core Development Team, R: A Language and Environment for Statistical Computing,
1470 (2014). <http://www.r-project.org/>.
- 1471 [61] D.W. Huang, B.T. Sherman, R.A. Lempicki, Systematic and integrative analysis of large
1472 gene lists using DAVID bioinformatics resources., *Nat. Protoc*. 4 (2009) 44–57.
1473 doi:10.1038/nprot.2008.211.
- 1474 [62] I. Fellows, Word Clouds, R Packag. Version 2.5. (2014). [http://cran.r-](http://cran.r-project.org/package=wordcloud)
1475 [project.org/package=wordcloud](http://cran.r-project.org/package=wordcloud).
- 1476 [63] A.A. Kalaitzis, N.D. Lawrence, A simple approach to ranking differentially expressed
1477 gene expression time courses through Gaussian process regression., *BMC Bioinformatics*.
1478 12 (2011) 180. doi:10.1186/1471-2105-12-180.
- 1479 [64] J. Schaefer, R. Opgen-Rhein, K. Strimmer, GeneNet: Modeling and Inferring Gene
1480 Networks, (2015). <http://cran.r-project.org/package=GeneNet>.

1481 [65] M.E.J. Newman, Finding community structure in networks using the eigenvectors of
1482 matrices, Phys. Rev. E - Stat. Nonlinear, Soft Matter Phys. 74 (2006).
1483 doi:10.1103/PhysRevE.74.036104.

1484

1485

1486 **Supplementary Information:**

1487 Supplementary File 1: Supplementary Text and Supplementary references (1-13)

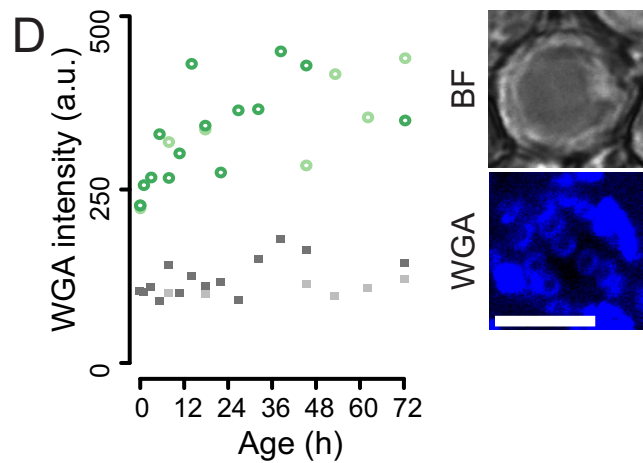
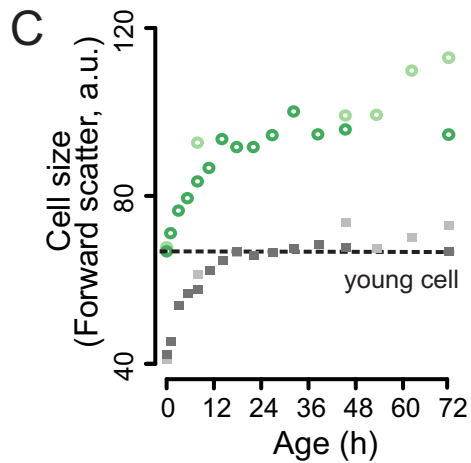
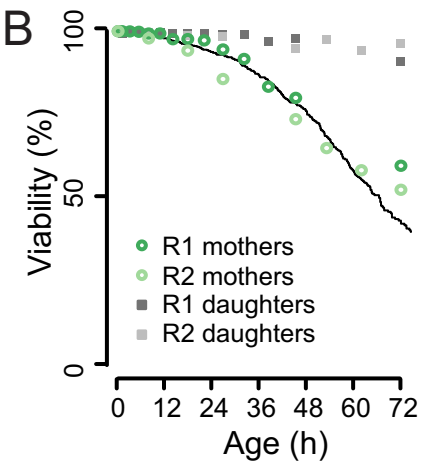
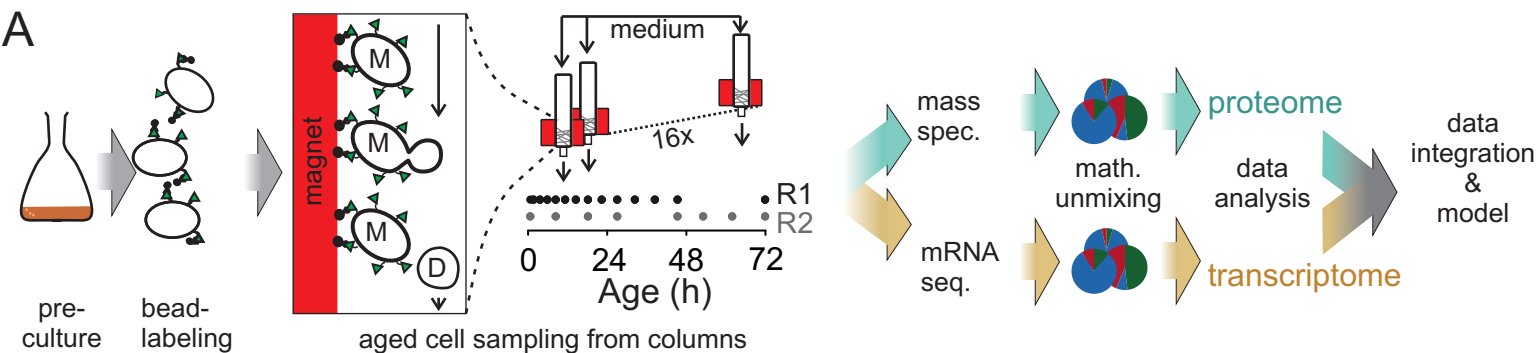
1488

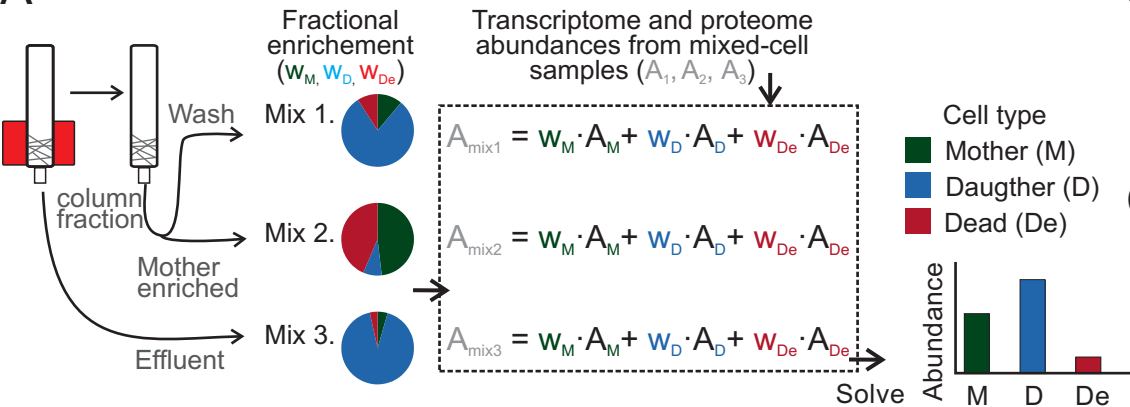
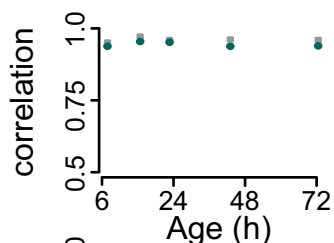
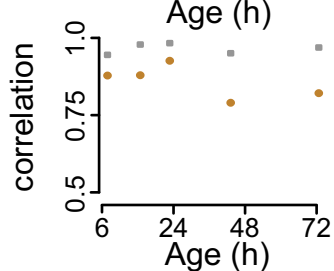
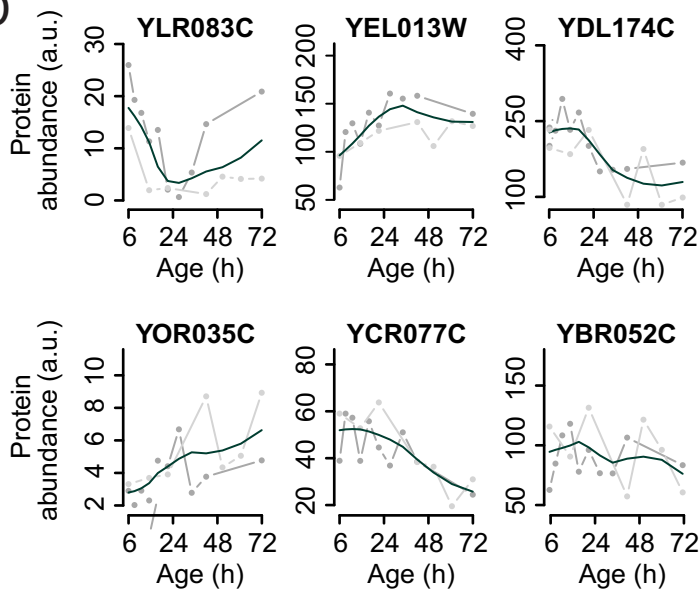
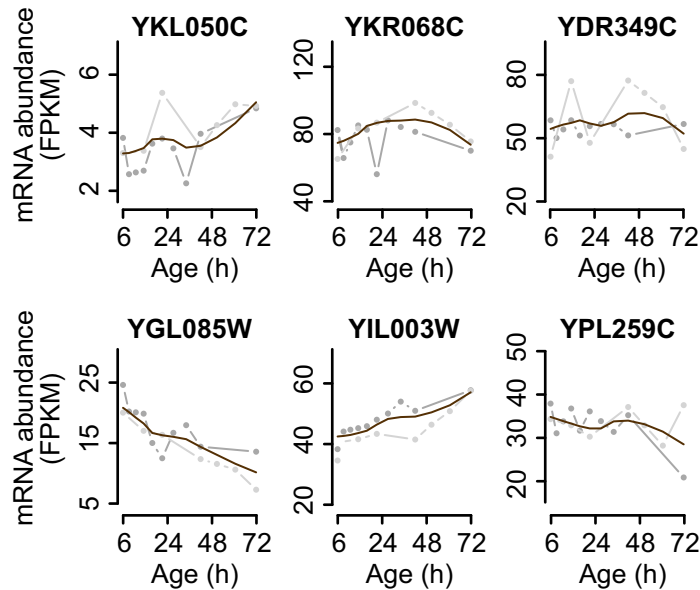
1489

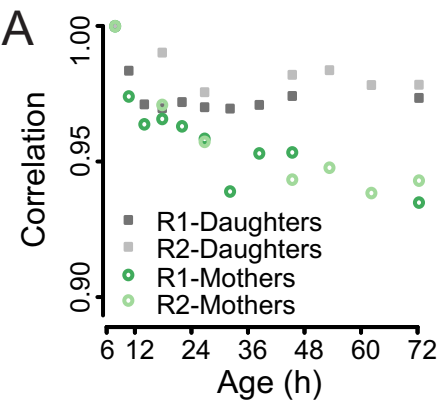
1490 **Acknowledgements:** We thank Hjalmar Permentier, and members of the Veenhoff, Chang and
1491 Heinemann laboratories for constructive discussions. We thank Yves Barral, Peter Lansdorp,
1492 Michael Chang and Christian Riedel for critical review of the manuscript. We thank Daphne
1493 Huberts for providing the time-based microfluidic lifespan curve of strain YSBN6. We also
1494 thank members of the Heinemann and Poolman laboratories and Stem Cell Technologies for
1495 their practical help with the experiments. This project was funded by the Netherlands
1496 Organization for Scientific Research (NWO; Systems Biology Centre for Energy Metabolism
1497 and Aging).

1498

1499

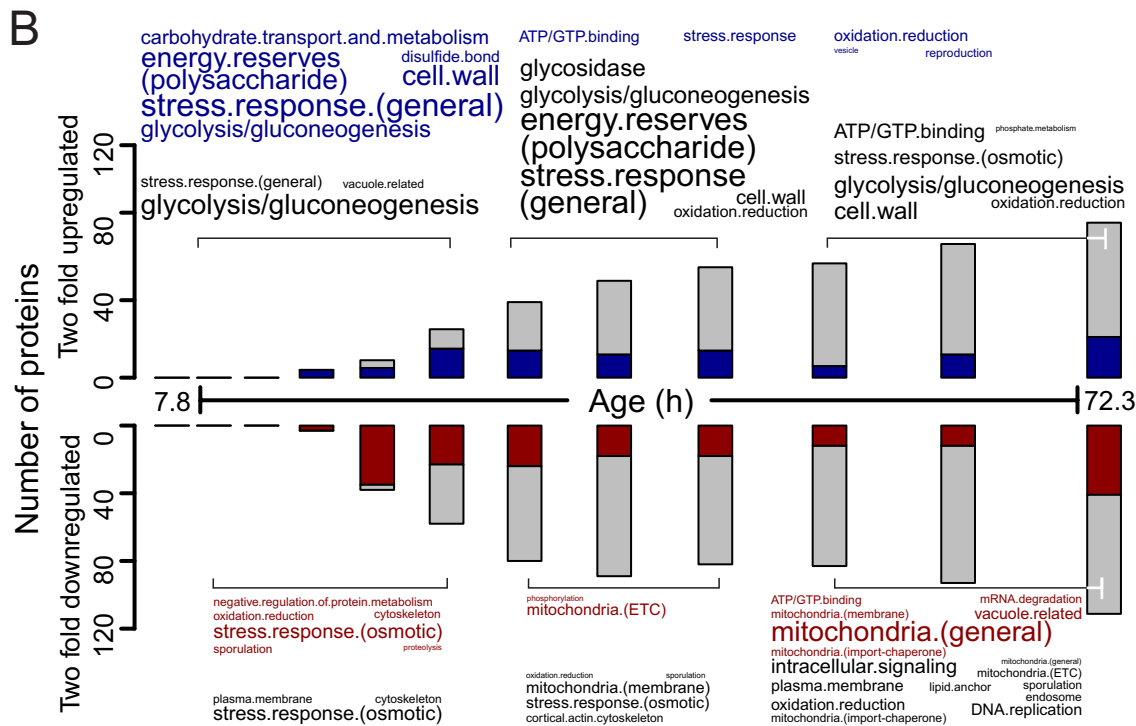


A**B****C****D****E**

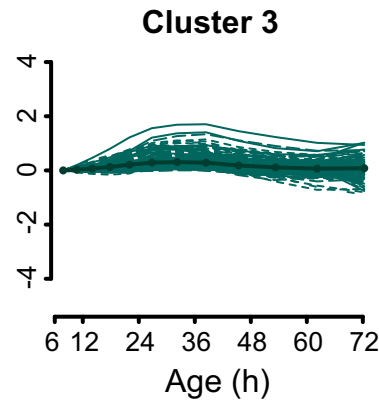
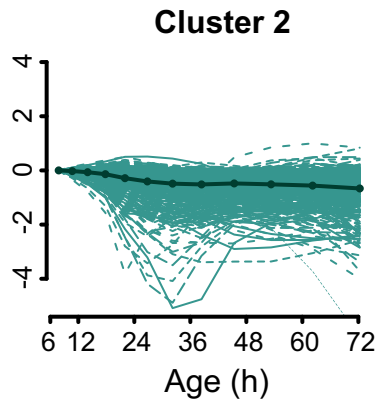
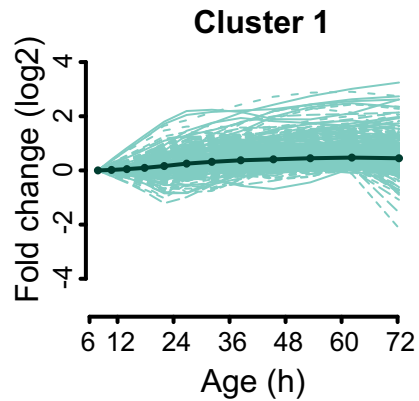
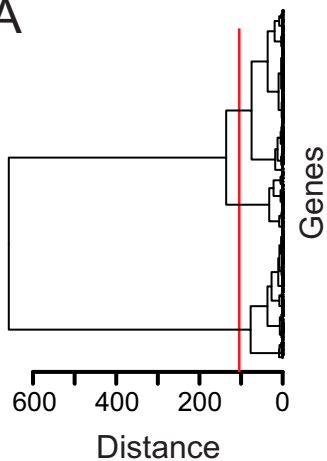


■ New changes up
 ■ New changes down
 ■ Previously changed

$0.5 < \text{Enrichment score} < 3.5$



A



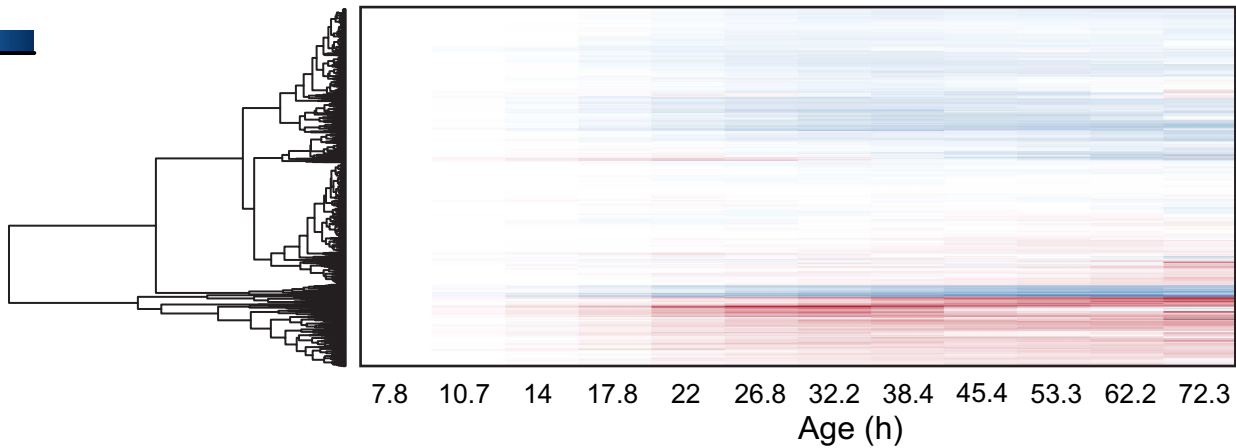
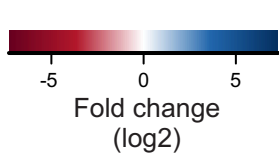
fatty.acid.metabolism
vacuole
translation.regulation
ATP/GTP.binding
ABC.transporteres

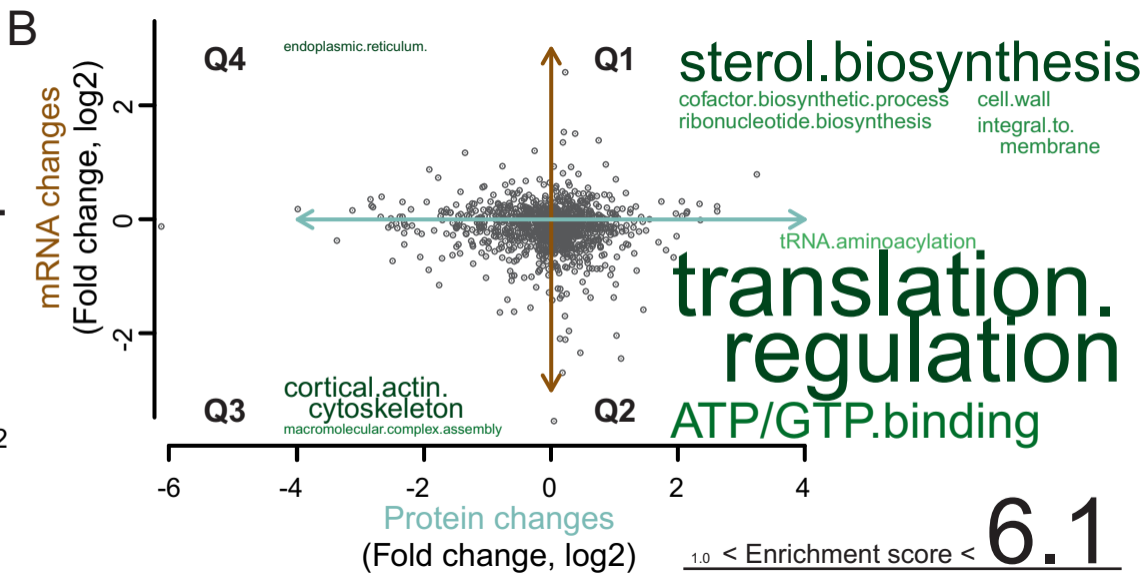
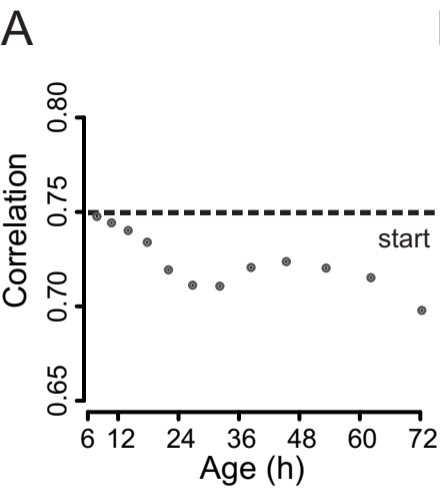
signal.peptides
disulfide.bond
apoptosis
unfolded.protein.binding
mitochondria.(general)
DNA.binding
amino.acid.biosynthesis

mitochondrial.(membrane)
heme.biosynthesis
integral.membrane
mitochondria.(general)
ribosomes
phospholipid.metabolism

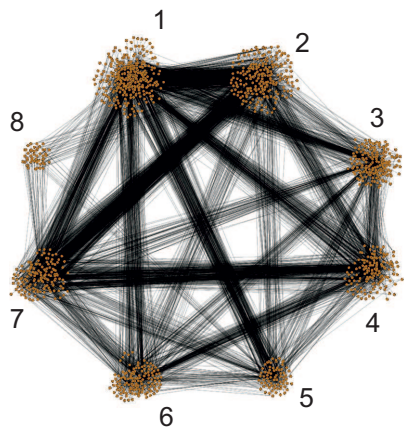
1.0 < Enrichment factor < 2.4

B

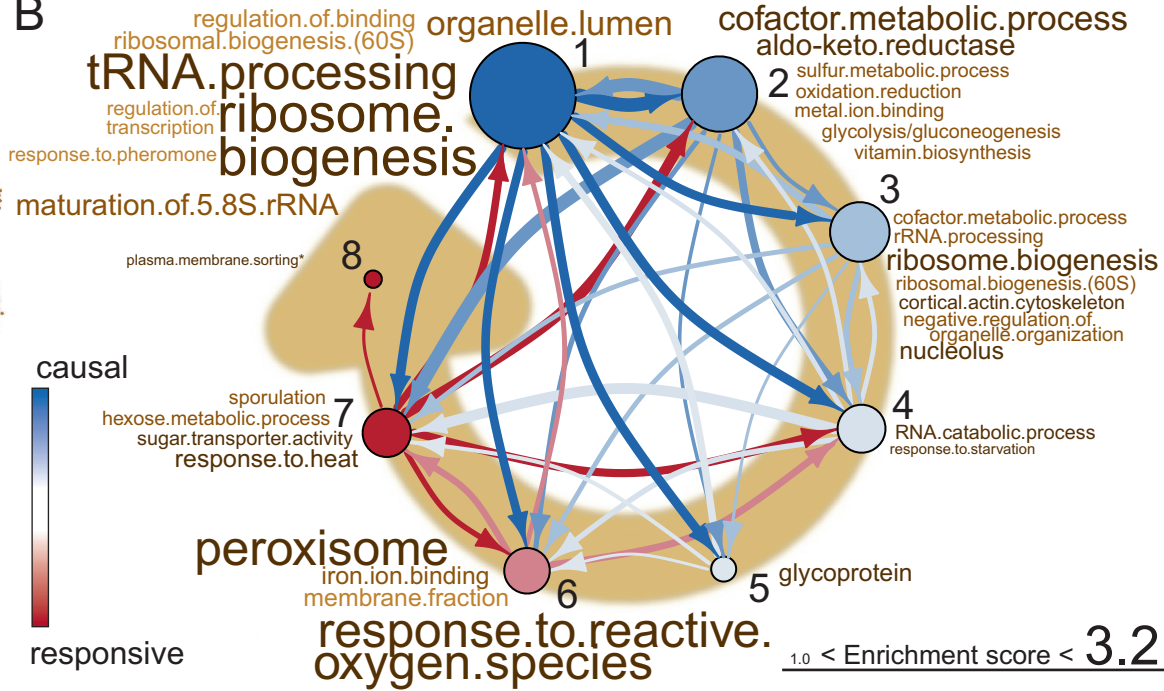




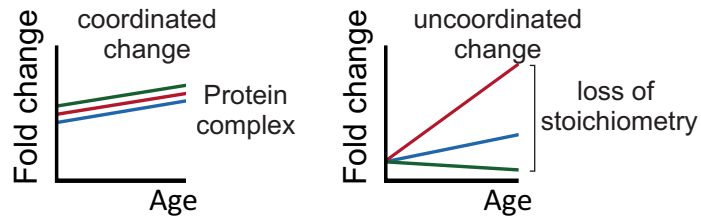
A



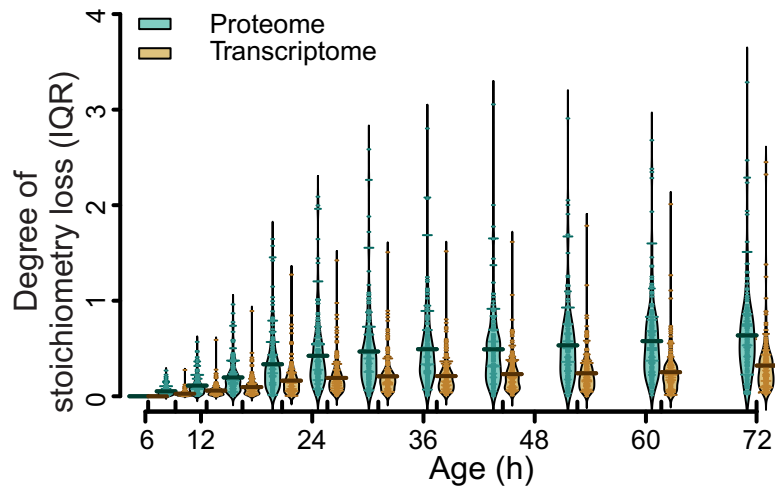
B



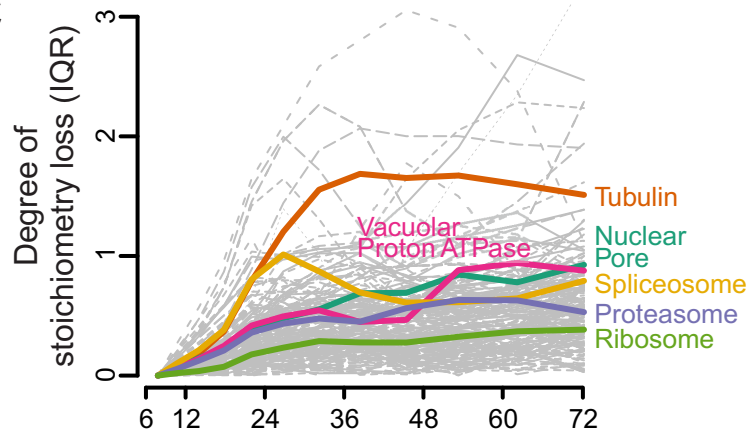
A



B



C



D

